CFD modelling of R410A flow through an Expansion Valve using Equilibrium and Modified Relaxation Models

Michal Loska[a], Jacek Smolka[a], Michal Haida[a,*], Ekaterini E. Kriezi[b], Krzysztof Banasiak[c]

[a]*Institute of Thermal Technology, Silesian University of Technology, Gliwice, Poland*
[b]*Danfoss Company, Nordborg, Denmark*
[c]*NTNU, Department of Thermal Engineering, Trondheim, Norway*

Abstract

The two-phase flow of R410A refrigerant through an electronic expansion valve (EEV) is modelled using two models, the Homogeneous Equilibrium Model (HEM) and Homogeneous Relaxation Model (HRM) in a CFD numerical analysis. The reason for this is to take a step towards developing a more generic description of two-phase flow calculations. The EEV, applied in air-conditioning and refrigeration systems, was examined by measuring the mass flow rate of the refrigerant, the pressure and the temperature at the valve inlet, and the pressure at the outlet. The EEV was regulated using pulse width modulation; however, during the experiments the EEV was fully opened. Operation of the valve was carried out over a sub-cooling range of 3.8 to 7.7 K. The expansion process started from around 20 bar and ended within the pressure range of 6.8 to 11.5 bar. The mass flow rates of the HEM are inaccurate when compared to the experimental results with a relative difference of approximately 42%. This outcome was expected because the theoretical background of the model assumes that there would be choking at saturation pressure. The modification of the HRM approach was performed with the use of a genetic algorithm (GA) in order to adapt the model's constants, originally defined for water, to R410A. The HRM approach from literature using constants for water yielded average differences of 17 and 26% using two different relaxation time correlations. The modified HRM approach produced an average relative difference of around 5% for optimised relaxation time correlation constants. The study proved the feasibility of the adaptation of the HRM approach to various working fluids, both synthetic and natural.

Keywords: Refrigeration, Expansion valve, Two-phase flow, CFD model, Relaxation model, Genetic algorithm

*Corresponding author. Institute of Thermal Technology, Silesian University of Technology, Konarskiego 22, Gliwice 44-100, Poland.

Email address: Michal.Haida@polsl.pl (Michal Haida)

1. Introduction

The basic function of an electronic expansion valve (EEV) in the refrigeration cycle is to maintain the pressure difference between the high and low-pressure sections of the cycle. Regulation of the refrigerant mass flow rate (MFR) is another essential function of the EEV as it allows the regulation of the cooling load. The MFR is usually regulated by the insertion of a needle into an orifice, and used as a as a variable expansion device which is shown in Fig. 1 (a). The deeper the needle is inserted, the lower the MFR produced. The needle inside the orifice creates a channel with a varying cross-section (CS) in a similar manner to a converging-diverging nozzle. Another way to regulate the flow is to pulsate the flow utilising a pulse width modulated valve, as shown in Fig. 1 (b). In this case, the MFR depends on how long it takes a plunger to close the EEV during one time period.

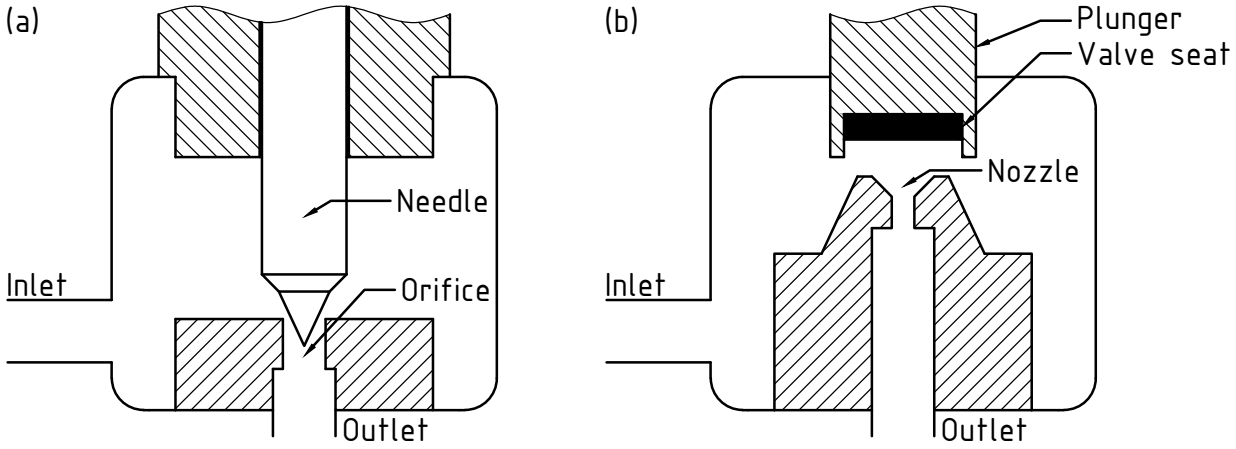

Figure 1: 1. (a) The EEV with the flow restricting needle and (b) the EEV with a periodically clogging plunger.

Fig. 1 shows the geometry of two EEVs considered converging and converging-diverging ducts which are usually found in EEVs. Flows inside the EEV, determined as compressible, single-phase fluids, are described thoroughly by the theory of gas dynamics, e.g. Zucker and Biblarz (2002). This also applies to the critical flow. The critical flow, or the choked flow, occurs when there is no further increase of the MFR with further reduction of the back-pressure. This is due to pressure disturbances propagating upstream with sonic velocity. If the velocity of the flow reaches the sonic velocity, the pressure disturbances cannot travel any further upstream (Elias and Lellouche, 1994; Moody, 1975). The only place where the single-phase fluid sonic velocity may occur in the converging and converging-diverging nozzle is at the minimum cross-section of the nozzle called the *throat*. If the pressure in the throat reaches the value providing the sonic velocity, any further reduction of the back-pressure will not affect the parameters within the throat and, consequently, the MFR. The aforementioned pressure which provides the sonic velocity is called the *critical pressure* and it should not be mistaken with the pressure corresponding to the critical point of the given fluid. For compressible single-phase flow, the critical pressure can easily be determined as a function of the stagnation pressure and the isentropic exponent.

There is no general equation describing the critical pressure, which is applicable to a wide range of conditions and fluids for a two-phase flow of one component. This fact makes the calculation of MFR for two-phase flow particularly difficult as the critical MFR results strictly from the critical pressure (Kolev, 2015). Moreover, for heterogeneous two-phase flow, the sonic velocity is no longer a thermodynamic property since it is dependent on the regime of the flow. This phenomenon has been shown in the experimental investigation made by Henry et al. (1971). Depending on the flow regime, e.g., slug flow, bubbly flow, separated flow, etc., the interfacial momentum transfer differs making the calculation of the sonic velocity for the mixture problematic. Other factors affecting two-phase flow are the mechanical and thermodynamic non-equilibria. A finite rate of momentum transfer between phases results in the mechanical non-equilibrium manifesting itself into a velocity difference between the phases. The thermodynamic non-equilibrium is a finite rate of heat and mass transfer between phases (Bilicki and Kestin, 1990), resulting in different temperatures for these phases. In other words, the phase change requires a finite time to occur and this time is called the *relaxation time*. The relaxation time is important during flow simulations through short channel paths such as orifices and nozzles. A fluid particle may transit a short channel path in a shorter time than the relaxation time. This results in the formation of a superheated (metastable) liquid at lower pressure than in those at thermodynamic equilibrium (Lahey and Moody, 1993) as the evaporation is delayed by the relaxation time, leading to a higher MFR than those predicted when assuming thermodynamic equilibrium. Sallet (1991) reported that the two-phase flow through a short nozzle or orifice, i.e., the flow affected by thermodynamic non-equilibrium effects, has an MFR which is two or three times higher than the flow through a long pipe with the same diameter as the short nozzle. This is because the pipe is a channel providing a residence time long enough to establish thermodynamic equilibrium. One of the models proposed by Sallet addressed two-phase water discharge from a vessel through a valve nozzle. For a vessel pressure equal to 689.5 kPa and a temperature range from 90 to 160 °C, MFRs resulting from this model were two to four times higher than MFRs resulting from the calculations assuming thermodynamic equilibrium. Tong and Tang (1997) reported a clear separation between flows through long channels and short channels. In long channels, thermodynamic equilibrium may be assumed, and in short channels, thermodynamic non-equilibrium effects must be considered.

The Homogeneous Equilibrium Model (HEM), and Homogeneous Relaxation Model (HRM) approaches find their applications in modelling the expansion process where a phase change occurs. This expansion process can be a leakage of flashing coolant from a ruptured pipe in the nuclear industry (Lahey and Moody, 1993), the discharge of compressed liquefied gases (Sallet, 1991), refrigerant expansion through ejectors (Haida et al., 2018), capillary tubes (Ingle et al., 2015), or EEVs. One of the main disadvantages of HEM is the presence of strong discontinuities of the sonic velocity at the saturation line. There is a significant difference between the sonic velocity for the liquid and the sonic velocity for the two-phase region, even for the vapour mass fraction approaching infinitely close to 0. There is an analogous difference between the sonic velocity for the vapour and the two-phase region, although it is not as severe as the aforementioned difference concerning the liquid saturation line. This discontinuity is in contradiction with the experimental data, according to Städtke (2006). Furthermore, Städtke presents graphs showing the sonic velocity differences for a two-phase mixture of water and steam over pressure ranges from 0 to 50 bar. This is illustrated in Fig. 2, where the vapour mass fraction is denoted by the x symbol.

In Fig. 2 (a) the difference between the sonic velocity for the liquid and for the two-phase region is presented. It can be seen, that the difference is enormous. Even at 50 bar, where the difference is the lowest, it still exceeds 1,000 m/s. The difference concerning the vapour is shown in Fig. 2 (b). It can be observed that for the liquid, sonic velocity difference decreases with increasing pressure, while for the vapour, the difference is seemingly constant over the whole pressure range.

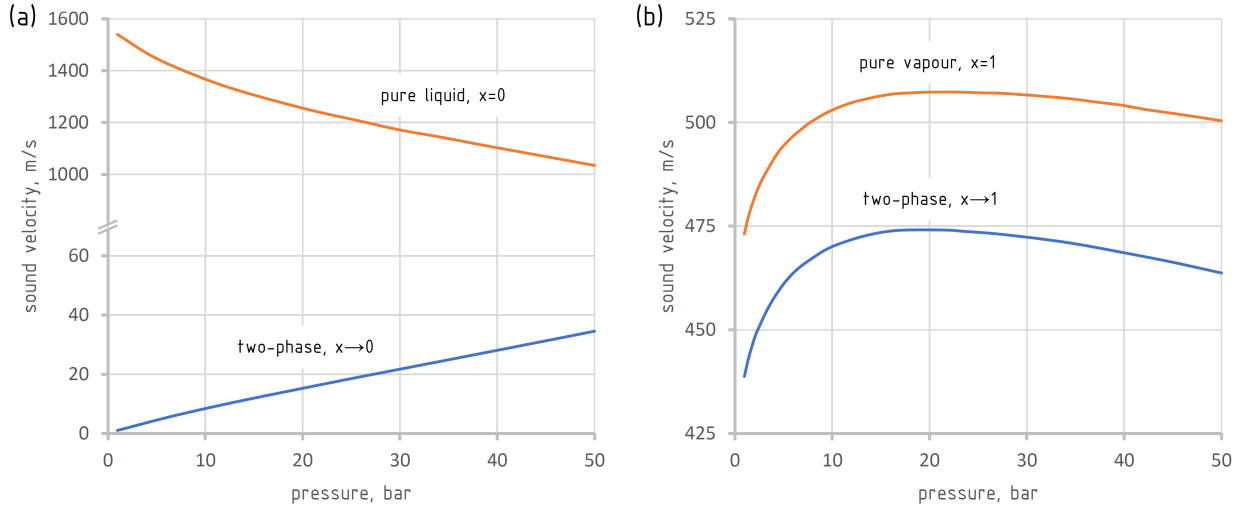

Figure 2: 2. The discontinuities of the HEM sonic velocity for (a) the liquid and (b) vapour saturation lines for H_2O (Städtke, 2006).

A significant discontinuity at the liquid saturation line is particularly unfortunate from the perspective of this study. An expansion line, resulting from the expansion process in the EEV, crosses the liquid saturation line. The liquid sonic velocity is so high that it is highly unlikely that the refrigerant in a liquid state will reach it while flowing through the EEV. Consequently, the liquid refrigerant may reach a higher velocity than the two-phase sonic velocity at the crossing of the expansion and the saturation lines. In this case, when the expanding refrigerant reaches the saturation line, the subsonic flow rapidly becomes supersonic, instantly choking the flow. This result from the HEM application is also reported by Städtke (2006). That author confirmed that the MFR in this case may be calculated by using a simple Bernoulli equation, Eq. (1).

$$\dot{m} = C_f A_{th} \sqrt{2\rho\left(T_o\right) \cdot \left[p_o - p_s\left(T_o\right)\right]} \tag{1}$$

where A_{th} is the cross-sectional area of the throat, C_f is the discharge coefficient for the incompressible liquid, and $\dot{m}$ is the mass flow rate. The subscripts o and s denote stagnation and saturation parameters, respectively.

Downar-Zapolski et al. (1996) presented a graph comparing the sonic velocities between HEM and HRM with respect to the void fraction for flashing water. This graph complements Städtke's graph in Fig. 2 and shows the advantage of HRM over HEM; the lack of sonic velocity discontinuities between single-phase and two-phase regions. As a result, the premature choking at the liquid saturation line will not appear, allowing for deeper expansion into the two-phase region. Hence, the MFR values calculated using HRM will be higher than those calculated using HEM.

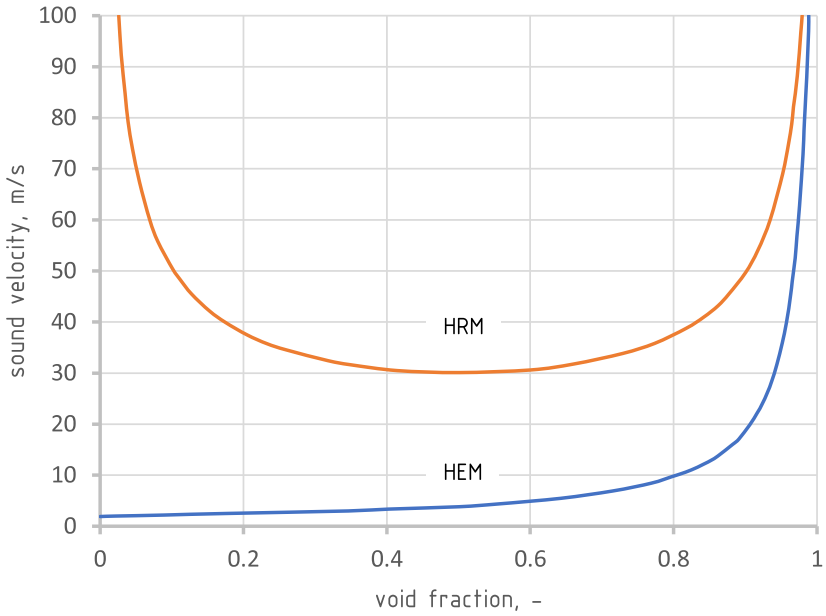

Figure 3: HRM and HEM sonic velocities for H_2O (Downar-Zapolski et al., 1996).

The work by Palacz et al. (2015) considered CO_2 flow through an ejector and discussed the accuracy of the HEM approach. Although it is a very specific application, this highlights the overall trend of the accuracy of HEM. The accuracy depends greatly on the operating conditions. The area close to the critical point had a very high accuracy, i.e., the MFR relative difference was approximately equal to 5%. However, a decrease in the temperature or the pressure negatively impacted the accuracy. The most reduced accuracy was found near the saturation line, where the relative differences reached up to 60%. In the work of Palacz et al. (2017a), the accuracy of HEM and HRM was given, again, for the CO_2 flow through an ejector. The HRM in the region close to the critical point provided the worst accuracy when compared to HEM and for some cases a relative difference that was twice as large as that from HEM. However, HRM provided improved accuracy in the regions where HEM had high relative differences. Unfortunately, the improvement was only 3-5 percentage points. Haida et al. (2018) considered the CFD simulation of CO_2 through an ejector and modified HRM empirical coefficients using optimisation methods to lower the discrepancy between computational and experimental data. There was an improvement of 4-19 percentage points from the HEM results. These points indicate that the empirical nature of HRM coefficients has a great impact on the MFR discrepancy and thus presents a chance for improvement.

The lack of any general theory behind two-phase flow means that there are numerous models predicting MFR. Geng et al. (2019) modelled the two-phase expansion of a R134A refrigerant in an ejector using a CFD approach. The metastability of the phase change was captured by adopting a finite rate phase change model developed by Yazdani et al. (2012). The resulting MFR was compared with the HEM and Abuaf and Henry-Fauske models. HEM yielded a 30% lower MFR, whilst Abuaf and Henry- Fauske models yielded a 20% higher MFR than Geng et al. (2019). Pourmahmoud et al. (2011) modelled the R410A and R22 flow through an EEV using

CFD by combining the HEM with the frozen flow model, with a coefficient capturing the effects of metastability. The resulting MFRs were close to the experimental results from the literature presented by Pourmahmoud et al. (2011). However, the ideal gas equation, not suited for two-phase flow, was used as an equation of state (EoS) without a comment. Grønheden (2015) investigated the R410A flow through the same EEV and for the same experimental data as in this manuscript, implementing HRM into the OpenFOAM software. Two correlations for the relaxation time containing empirical constants for water yielded relative differences of 30% and 10% for MFR, with respect to the experimental data. Attou and Seynhaeve (1999a,b) modelled the thermodynamic non-equilibrium two-phase flow by improving the 1-D Delayed Equilibrium Model (DEM). The metastability was taken into account by introducing the vaporisation index which was a mass fraction of the metastable liquid in a two-phase mixture. The DEM improvement considered a closing equation for vaporisation index modification, so the model has a good prediction of MFR for inlet conditions close to the saturated liquid line. The model was used to simulate water-steam flow through a pipe with abrupt enlargement.

For a sub-cooled liquid at the inlet, DEM and HEM provided MFRs with average relative errors from the experimental results equal to 2.5% and approximately 17%, respectively. For the two-phase region near the liquid saturation line with vapour mass fraction up to 6%, DEM and HEM provided MFRs with average relative errors from experimental results equal to 4% and approximately 28%, respectively. Saleh and Aly (2016) developed an artificial neural network (ANN) to calculate the MFR for R22, R407C and R410A flowing through an EEV. The agreement between calculated MFRs and the experimental MFRs were 0.7%, 1.1% and 0.006% for R22, R407C and R410A, respectively. A general model considering all three refrigerants provided good agreement of approximately 2.5%. Cao et al. (2016) presented an ANN predicting a MFR for R410A, R407C and R22 flowing through an EEV. The ANN with a Tan-Sigmoid transfer function provided an average deviation of -0.4%, 0.1% and 0.1%, respectively compared to their in-house experiment, literature data and manufacturers' data. Analogously, the ANN with an x^3 transfer function provided an average deviation of -0.2%, 0.07% and -1.1%, respectively. By experiment, Chen et al. (2019) examined the MFR of a R1233ZD refrigerant flowing through an EEV by creating an ANN and power-law correlation model. The ANN and the power-law correlation model provided results with a -0.2% and 0.8% average deviation, respectively. In another study, Chen et al. (2017) created a power-law and polynomial correlation returning an MFR of the R245FA flow through an EEV. The average deviations were 0.58% and 0.77% for the polynomial correlation and power-law, respectively. In the next study, Chen et al. (2018) expanded the R245FA flow investigation by using an additional three EEVs with larger orifice diameters, and the resulting average deviations were 0.67% and 0.85% for the power-law and polynomial correlation, respectively. Zhifang et al. (2008) developed a mass flow correlation for R134A flow through an EEV characterised by a maximum error of 6.8%. Li (2013) investigated experimental data from the literature for R22, R407C and R410 flow through an EEV. Based on the experimental data, a polynomial correlation and an empirical correlation resulting from the Buckingham π-theorem were developed to predict MFR. For the R410A the relative error ranges for the polynomial correlation and the empirical correlation were $\langle -5\%,\ 5\% \rangle$ and $\langle -15\%,\ 15\% \rangle$, respectively. In the literature, there is a significant amount of work which addresses empirical correlations for MFR for numerous refrigerants flowing through an EEV. Empirical correlations

concerning R410A from Shanwei et al. (2005), Park et al. (2007) and Chen et al. (2009) provided the relative deviations in the following ranges: $\langle -10.6\%,\ 9.9\% \rangle$, $\langle -15\%,\ 15\% \rangle$ and $\langle -7\%,\ 10\% \rangle$, respectively.

The ANN, power-law correlation and polynomial correlation models, while being practical, ignore the physics of the process and rely only on the empirical data, fitting the coefficients to approximate MFR ranges with the parameters limited by the measurement scope and working fluid used. The CFD approach requires a longer computational time than the above-mentioned empirical correlations, providing not only the predicted MFR itself but also the physical background in the form of field results with many parameters. Such results are interesting from a scientific point of view since they broaden the knowledge of two-phase phenomena, and from a practical point of view, since they can suggest new solutions in, e.g., the design or improvement of the operation effectiveness of a particular device. However, there is a scarcity of research considering CFD modelling of two-phase flow through EEVs. In this work, not only is the CFD model of two-phase flow through an EEV presented, but a procedure for adapting this method to many media is also presented.

The main objective of this work is to propose a CFD model of R410A refrigerant flow through the AKV 10-2 model EEV. The HEM and HRM approaches are used to capture the generation of the vapour during the phase change. The CFD model is used to predict the MFR of R410A for a valve nozzle with an inlet pressure of approximately 20 bar for every operation point; the outlet pressure is varied from 6.8 to 11.5 bar, and the sub-cooling range is 3.8 to 7.7 K according to experimental tests carried out at the Danfoss laboratory. The valve nozzle was fully opened for all operating conditions, since it allows for the most accurate acquisition of experimental data. The CFD model will provide the distribution of thermodynamic parameters throughout the EEV geometry that allow for a deeper understanding of metastability phenomena occurring inside the valve. The 2-D or 3-D distribution of thermodynamic parameters results in global parameters, e.g., the pressure drop and MFR which can be used to assess the quality of the design of an expansion device.

The distribution of thermodynamic parameters allows for the study of geometry effects on valve performance that would not be revealed by other modelling approaches, e.g., flow separation, formulation of recirculation zones and near wall flow behaviour. Moreover, an analysis of such distributions allows for the calculation of the distribution of the entropy generation that can directly localise regions where the potential for the design improvement exists. A CFD model providing such results is a convenient tool for design purposes because it allows for the shape design and optimisation of the expansion valve. Due to this fact, the HRM model was selected in the current study, as it provides a shorter computational time in comparison to the mixture approach proposed by Yazdani et al. (2012), as reported by Lee et al. (2016), making the HRM model more convenient in the further design optimisation of an expansion device. It has to be noted, however, that Yazdani's mixture approach was successfully implemented in the work of Bodys et al. (2020) where a more complex flow was simulated through a novel design of a CO_2 ejector with a by-pass duct of the suction flow. In addition, Yazdani's approach was implemented in the work of Geng et al. (2019), mentioned earlier, concerning the R134A converging-diverging nozzle, while a similar approach to Yazdani was adopted in the work of Baek et al. (2018) who used a R134A ejector. The HRM empirical coefficients for water derived by Downar-Zapolski et al. (1996) were

replaced as a result of the optimisation procedure adapting the HRM approach to the R410A refrigerant which minimised the discrepancy between the calculated results and the experimental data. The optimisation procedure was based on a genetic algorithm (GA) and allowed for the reduction of the MFR relative difference from 26% to 5%. This procedure would be a relatively simple way to adapt the HRM approach from water to different working fluids.

2. EEV geometry and mesh

2.1. Geometry

The EEV being studied here has a geometry containing a clogging plunger. Because a fully open valve is being studied, there is no need to capture the movement of the plunger during the geometry generation, so the whole grid is modelled as if it were stationary. Danfoss provided a 3-D geometry file containing an assembly of components of the AKV 10-2 model EEV. The actual feature of the valve flow channels used in the study was simplified to a fully axisymmetric geometry in the mathematical model. In the work regarding the flow modelling through an ejector, Palacz et al. (2016) reported that the motive nozzle mass flow rate for 2-D axisymmetric geometry has a negligible difference to the 3-D MFRs by 0.14 percentage points. Pianthong et al. (2007) presented the static pressure distribution along an ejector for 2-D and 3-D geometry, concluding that the properties from 2-D geometry are satisfactorily close to the ones from the 3-D geometry. One must note, that the 2-D axisymmetric simplification of an ejector geometry has the most significant impact on the inlet channel to the suction nozzle. The final version of geometry, presented in Fig. 4, was expanded in an axial direction, to maintain the value of inlet cross-section area of the original assembly. The length of the additional inlet channel was chosen to exceed ten hydraulic diameters so a well-developed flow profile could be acquired. In addition, the outlet section with the biggest diameter was omitted to delete the recirculation area where the vortices would form. Due to this, the stability of the calculations increased. Grønheden (2015) verified that the assumption of neglecting the outlet section tends to have an insignificant impact on the overall results.

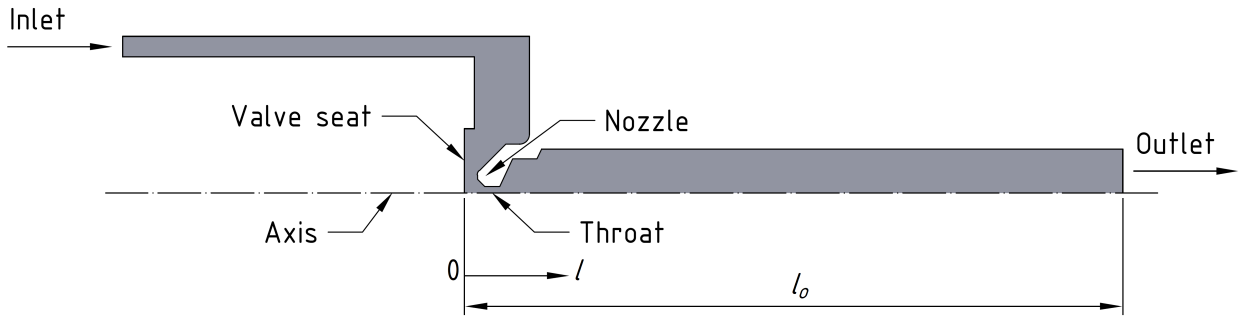

Figure 4: The final version of 2-D valve geometry.

2.2. Mesh

Six meshes of quadrilateral cells were generated with numbers in the range from 12,000 to 400,000. The exact number of cells can be found in Table 4, which contains the results of the mesh independence study for the HEM calculations described in Section 4.2. Three of the characteristic grids in a few selected EEV areas can be seen in Fig. 5. As the MFR prediction is the main result of the model, the throat area had the most refined mesh with the aspect ratio close to 1. For even more precise results considering irreversible phenomena, areas where the flow separation occurs should be as refined as the throat area. However, this was not the aim of the current study.

3. Mathematical model

3.1. The HEM approach

The main assumptions of the model are the mechanical and thermodynamic equilibria, which imply that the phases share the same temperature and velocity. Furthermore, the equality of pressure between the phases is assumed. In other words, HEM assumes an infinite rate of heat, mass and momentum transfer between phases.

The governing equations solved in this model (Anderson, 1995) are the mass, momentum and energy conservation equations defined in Eqs (2)-(4). Steady state conditions were considered, hence the lack of all-time derivatives. Eq. (2) is defined:

$$\nabla \cdot (\overline{\rho}\widetilde{\boldsymbol{u}}) = 0 \tag{2}$$

where ρ is the density and $\boldsymbol{u}$ is the velocity vector. The overline ($\bar{}$) and the tilde ($\tilde{}$) above the symbols denote the Reynolds-averaged and Favre-averaged quantities, respectively. Eq. (3) is defined:

$$\nabla \cdot (\overline{\rho}\widetilde{\boldsymbol{u}}\widetilde{\boldsymbol{u}}) = -\nabla \overline{p} + \nabla \cdot (\overline{\boldsymbol{\tau}} + \boldsymbol{\tau}_{\boldsymbol{turb}}) \tag{3}$$

where p is the pressure, $\boldsymbol{\tau}$ is the stress tensor and $\boldsymbol{\tau}_{\boldsymbol{turb}}$ is the turbulent stress tensor. Eq. (4) is defined:

$$\nabla \cdot \left(\overline{\rho}\widetilde{\boldsymbol{u}}\widetilde{E}\right) = \nabla \cdot \left[\left(\frac{\lambda}{\frac{\partial \widetilde{h}}{\partial \overline{T}}}\right)_p \nabla \widetilde{h} + \overline{\boldsymbol{\tau}} \cdot \widetilde{\boldsymbol{u}}\right] \tag{4}$$

where E is the total specific enthalpy, λ is the thermal conductivity, h is the specific enthalpy and T is the temperature.

The energy equation formulation originates from the work of Smolka et al. (2013). In the current study, the range of operation parameters used is located mostly in the two-phase region where the temperature and the pressure are strictly bound together and cannot be used as independent quantities. To amend this, Smolka et al. (2013) proposed the aforementioned energy equation, Eq. (4) based on a specific enthalpy instead of the temperature. Thus, after implementation of this equation as the User-Defined Scalar (UDS) feature to ANSYS Fluent (ANSYS, Inc., 2011), the specific enthalpy and pressure can serve as independent variables in the single and two-phase regions. Those variables were used to define the fluid properties as a function described in Eq. (5).

$$\{\rho,\ \mu,\ \lambda,\ c_p\} = f\,(p,\ h) \tag{5}$$

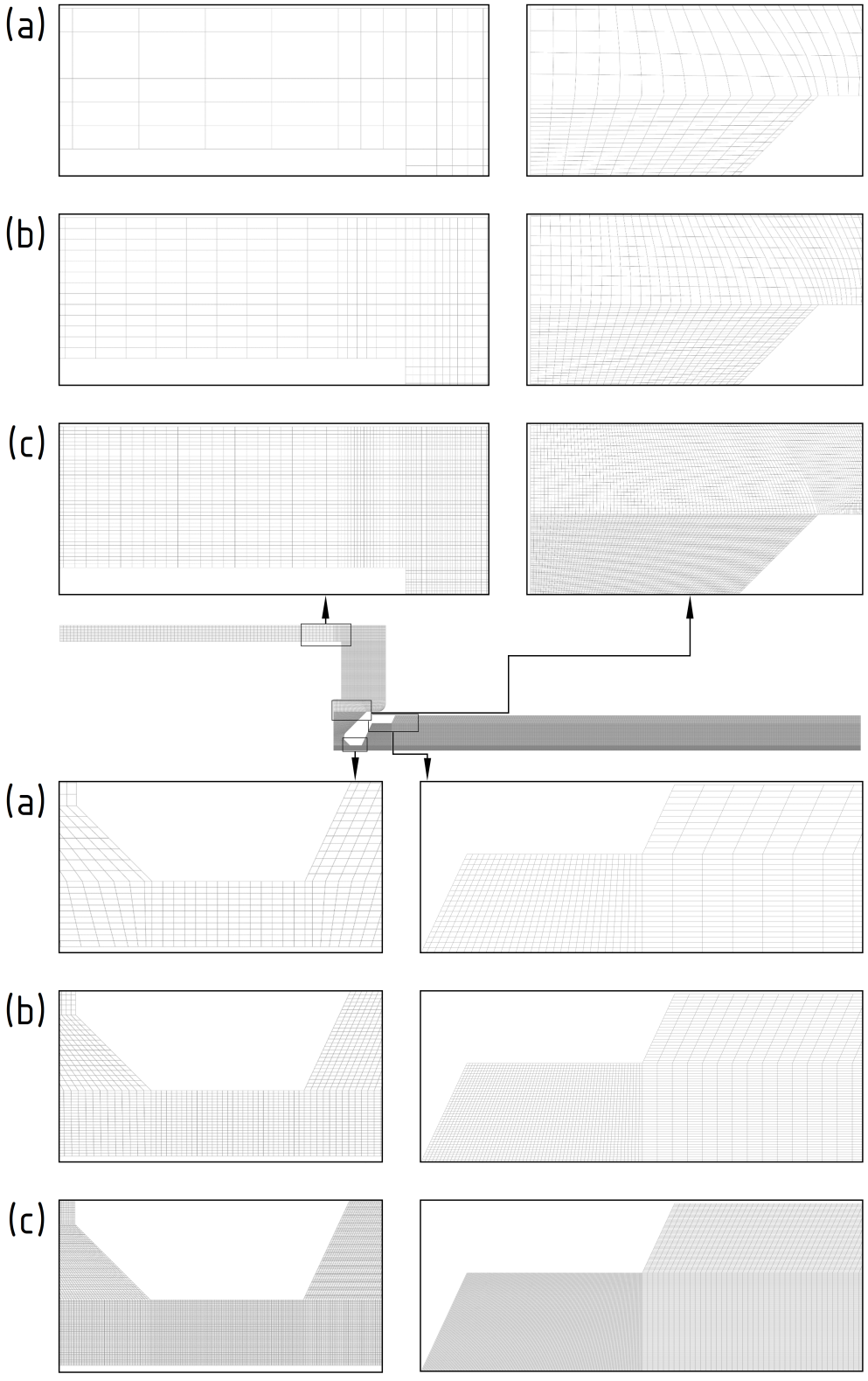

Figure 5: Meshes (a) no 1, (b) no 3 and (c) no 6 with 12, 51 and 412 thousand cells, respectively.

where μ is the dynamic viscosity and c_p is the specific heat capacity.

The properties' values were invoked as functions of the pressure and the specific enthalpy, as defined in Eq. (5), from a lookup-table for properties generated from the REFPROP 9.0 property equations, (Lemmon et al., 2010).

3.2. The HRM approach

HRM, as with HEM, assumes the equality of the phase velocities and pressures. However, HRM captures the thermodynamic non-equilibrium by introducing a concept of relaxation time, described in Section 1.

The governing equations of HRM comprise of all the conservation equations listed as Eqs (2)-(4). In addition, Eq. (6) which defines the vapour mass balance presented by Downar-Zapolski et al. (1996) was implemented in the same manner as Eq (4), using the User-Defined Scalar feature. More details about the UDS implementation can be found in the works of Haida et al. (2018) and Palacz et al. (2017a). This equation defines the rate of vapour generation, delayed by thermodynamic non-equilibrium effects:

$$\frac{\mathrm{D}\widetilde{x}}{\mathrm{D}t} = \frac{\widetilde{\Gamma}}{\overline{\rho}} = -\frac{\widetilde{x} - \widetilde{x}_{eq}}{\widetilde{\theta}} \tag{6}$$

where x is the instantaneous vapour mass fraction affected by the metastability, t is the time, Γ is the vapour generation rate, x_{eq} is the equilibrium vapour mass fraction and θ is the relaxation time. Downar-Zapolski et al. (1996) developed two correlations for θ. The first correlation for the relatively low pressures (up to 10 bar) for water was defined in Eq. (7):

$$\widetilde{\theta} = \theta_{0,\,lp}\, \widetilde{\alpha}^{a_{lp}} \overline{\psi}^{b_{lp}} \tag{7}$$

where $\theta_{0,\,lp}$ is the reference relaxation time equal to $6.51 \cdot 10^{-4}$ s, α is the void fraction, a_{lp} is the void fraction exponent equal to -0.257, ψ is the non-dimensional pressure difference defined in Eq. (8) and b_{lp} is the non-dimensional pressure difference exponent equal to -2.24. Eq. (8) is defined:

$$\overline{\psi} = \left| \frac{\overline{p}_s\,(T_{in}) - \overline{p}}{\overline{p}_s\,(T_{in})} \right| \tag{8}$$

where T_{in} is the inlet temperature.

The second correlation for the relaxation time for the water flow at relatively high pressures (above 10 bar) was used giving Eq. (9):

$$\widetilde{\theta} = \theta_{0,\,hp}\, \widetilde{\alpha}^{a_{hp}} \overline{\phi}^{b_{hp}} \tag{9}$$

where $\theta_{0,\,hp}$ is the reference relaxation time equal to $3.84 \cdot 10^{-7}$ s, a_{hp} is the void fraction exponent equal to -0.54, ϕ is the non-dimensional pressure difference modified by Angielczyk et al. (2010) and b_{hp} is the non-dimensional pressure difference exponent equal to -1.76.

$$\overline{\phi} = \left| \frac{\overline{p}_s\,(s_{in}) - \overline{p}}{p_c - \overline{p}_s\,(s_{in})} \right| \tag{10}$$

where s_{in} is the inlet specific entropy and p_c is the pressure corresponding to the critical point.

The above-mentioned modification was used to replace the inlet temperature defining the saturation pressure with the specific entropy. As a result, the non-dimensional pressure difference could be calculated even if parameters at the inlet were in the critical region. In the following sections, the exponents from Eqs (7) and (9) along with the reference relaxation time will be described as the HRM parameters.

The void fraction in Eqs (7) and (9) is defined in Eq. (11):

$$\widetilde{\alpha} = \frac{\widetilde{x} \cdot \overline{\rho}}{\overline{\rho_v}} \tag{11}$$

where the subscript v is the vapour saturation line property. The properties on liquid and vapour saturation lines are defined as a function of pressure, as described in Eq. (12):

$$\{\rho_v,\ \rho_l,\ \mu_v,\ \mu_l,\ \lambda_v,\ \lambda_l,\ c_{p_v},\ c_{p_l},\ h_v,\ h_l\} = f\,(p) \tag{12}$$

where the subscript l is the liquid saturation line property.

In the two-phase region, Eq. (5) is insufficient to capture the properties of metastable fluid. For this reason, the properties of a metastable fluid are defined in Eq. (13).

$$\{\rho,\ \mu,\ \lambda,\ c_p\} = f\,(p,\ h_{ml}) \tag{13}$$

where the subscript ml is the property in metastable conditions.

The specific enthalpy in metastable conditions, h_{ml} was calculated using the specific enthalpy and vapour mass fraction from governing equations (4) and (6) as defined in Eq. (14).

$$\widetilde{h} = \widetilde{x}\widetilde{h_v} + (1 - \widetilde{x})\,\widetilde{h_{ml}} \tag{14}$$

Eq. (15) defines the calculation of the density in metastable conditions and serves as an example since every other property under metastable conditions were calculated in an analogical manner. Eq (15) is defined:

$$\frac{1}{\overline{\rho}} = \widetilde{x}\frac{1}{\overline{\rho_v}} + (1 - \widetilde{x})\,\frac{1}{\overline{\rho_{ml}}\left(\overline{p},\ \widetilde{h_{ml}}\right)} \tag{15}$$

The properties' values were acquired from the lookup-table for properties as described in Section 3.1.

3.3. Turbulence model

The lack of turbulence model screening in the scope of this study was compensated by the literature review which is summarised in Table 1. Table 1 comprises works where the turbulence models were investigated to simulate the ejector operation for fluids listed in the second column. The quantities used to assess global performance are listed in the third column. The last columns comprise relative errors between the calculated global quantity and experimental data. Relative errors from Croquer et al. (2016) study consider models with a high-Reynolds number. The only error presented for a model with a low-Reynolds number formulation was for $k-\omega$ SST and was

equal to 5.7%. Regarding Varga et al. (2017) study, case with experimental back pressure set as an outlet boundary condition was named Variant 1 and the case with calculated back pressure set as an outlet boundary condition was named Variant 2. The final recommendations in those works were proposed basing not only on accuracy of the global quantity calculation, but also on local distribution of thermodynamic parameters and advantages such as independence from wall treatment. The most of the authors concluded that $k-\omega$ SST was the best, except Varga et al. (2017), who concluded that Transition SST model was the best. The Realizable $k-\epsilon$ provides larger relative errors than $k-\omega$ SST by, on average, 0.6 percentage points, excluding the Varga et al. (2017) outlier case for the experimental back pressure with severe underestimation of COP, which is a negligible value difference. One must note, that Mazzelli et al. (2015) considered single-phase air flow, while the rest of the presented turbulence model investigations were devoted to the ejectors with saturated vapour at the inlet of the motive nozzle, which is contrary to the condition considered in current manuscript which is sub-cooled liquid at the EEV inlet. The works of Geng et al. (2019), Rusly et al. (2005) and Ingle et al. (2015) are devoted to expansion devices with similar inlet conditions as in current manuscript. The Realizable $k-\epsilon$ turbulence model was used in the work of Geng et al. (2019). The authors considered the modelling of the two-phased expansion of a refrigerant flowing through a converging-diverging nozzle inside an ejector. The same turbulence model was used by Rusly et al. (2005) in a CFD investigation of several ejector designs in a combined ejector cooling system. Moreover, Ingle et al. (2015) used the Realizable $k-\epsilon$ turbulence model to simulate the flow through a capillary tube. With regards to the fact that the above devices are similar to an EEV, the Realizable $k-\epsilon$ model with wall treatment set as the *Standard Wall Function*, was employed in the numerical part of this study. The transport equations introduced by the turbulence model are defined in the ANSYS Fluent manual (ANSYS, Inc., 2011). The model constants values were maintained at the default level.

3.4. Boundary conditions

The experimental study of R410A flow through an EEV was completed at the Danfoss laboratory in Denmark. Table 2 includes all the experimental data from the test rig. The data in the columns are as follows:

- the operating point (OP),
- the mass flux,
- the inlet pressure,
- the inlet temperature,
- the outlet pressure.

The mass flux, $\dot{g}$, is defined in Eq. (16):

$$\dot{g} = \frac{\dot{m}}{A_{th}} \tag{16}$$

For the equipment used, the accuracy was ±0.15% of the measured value for the Siemens Sitrans FC Mass 2100 Di 6 flowmeter, ±0.05% of the selected range of measured values for Wika P-10 manometers and ±0,44 K and ±0,03 K for the measurement at the EEV inlet and outlet for

Table 1: Continued summary of turbulence models literature review.

Author	Fluid	Examined global quantity		Relative error, % Spalart-Allmaras	Standard $k-\epsilon$	RNG $k-\epsilon$	Realizable $k-\epsilon$
Besagni and Inzoli (2017)	H_2O	Entrainment ratio		1.94	12.94	0.97	2.27
Croquer et al. (2016)	R134A	Entrainment ratio		-	4.27	6.03	8.79
Varga et al. (2017)	H_2O	COP	Variant 1	-	33.00	26.00	42.00
	H_2O	COP	Variant 2	-	8.20	7.67	11.60
Mazzelli et al. (2015)	Air	Entrainment ratio		-	27.10	-	28.52

Author	Fluid	Examined global quantity		Relative error, % Standard $k-\omega$	$k-\omega$ SST	RSM	Transition SST
Besagni and Inzoli (2017)	H_2O	Entrainment ratio		11.65	1.94	11.65	-
Croquer et al. (2016)	R134A	Entrainment ratio		-	6.78	-	-
Varga et al. (2017)	H_2O	COP	Variant 1	-	72.00	-	4.33
	H_2O	COP	Variant 2	17.93	12.27	-	4.53
Mazzelli et al. (2015)	Air	Entrainment ratio		-	27.85	27.63	-

Danfoss AKS21 PT1000 thermometers, respectively. The accuracy for the calibration equipment was ±0.12% of the measured value for the flowmeter, ±2 kPa for the manometers and ±0.08 K for the thermometers. The data from the last three columns were used to define the boundary conditions. As explained in Section 3.1, the independent variables used in the calculations are the specific enthalpy and the pressure. The inlet parameters from Table 2 are sufficient to acquire the specific enthalpy and to define the boundary conditions with parameters appropriate to the adopted governing equations. Hence, the inlet boundary condition was set to the pressure-inlet and defined by the aforementioned inlet specific enthalpy and inlet pressure. The outlet boundary condition was set as the pressure-outlet and defined by the outlet pressure measurement. The mass flux measurements were used to validate the numerical model.

The general location of the eight OPs on the pressure-enthalpy graph are given in Fig. 6 (a). The red marking above the rectangle is the location of all the inlet conditions. The inlet conditions are fairly similar for every OP. The parameter that differs the most between the OPs is the outlet pressure, i.e. the parameters at which the expansion process ends. The bold, green rectangle indicates the expected area where the expansion process ends for all the OPs. The exact location of each of the eight OPs can be seen in the scaled-up pressure-enthalpy graph given in Fig. 6 (b). It can be seen that OPs that are seemingly similar in terms of pressure range, e.g., OP6 and OP7,

Table 2: Experimental data provided by Danfoss.

OP	$\dot{g}$, kg s^{-1}m^{-2}	p_{in}, Pa	T_{in}, K	p_{out}, Pa
1	30,956	1,965,000	300.9	1,151,000
2	32,488	1,966,000	300.9	1,086,000
3	34,330	1,963,000	301.2	936,000
4	36,272	1,965,000	301.2	807,000
5	38,013	1,965,000	301.5	682,000
6	34,807	1,963,000	298.9	936,000
7	34,673	1,963,000	297.1	935,000
8	31,567	1,967,000	297.0	1,142,000

are actually different due to the inlet specific enthalpy.

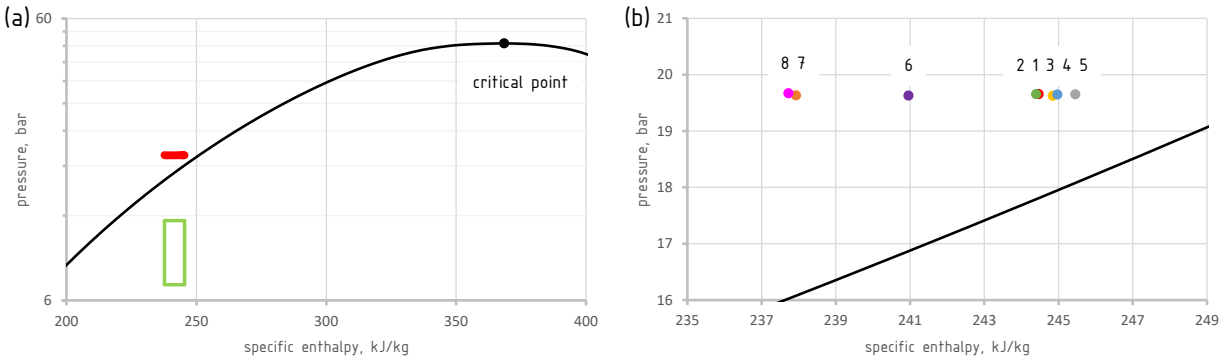

Figure 6: (a) Inlet (red marking) and outlet (green frame) boundary conditions and (b) a scaled-up view showing the inlet boundary conditions on the pressure-enthalpy diagram.

3.5. Material properties

The geometry only comprises of the R410A refrigerant. The refrigerant was modelled as a real fluid with its properties lookup-table generated based on the REFPROP property equations. The intervals between the lookup-table points were 5.34 kPa and 0.9 kJ/kg for the pressure and the specific enthalpy, respectively. The properties corresponding to the pressure and the specific enthalpy values between the points were interpolated using bilinear interpolation functions between input parameters. The size of the lookup table was defined for 500 point of each input parameter. Hence, throughout the operating regime of EEV was within the properties table at interpolation discrepancy within ±0.1% when compared to results given directly from the REFPROP database. The roughness of the wall was unknown, and for this reason, its effect on the MFR was investigated. The HRM results of the investigation are given in Table 3. The first column contains the OPs and the following four columns contain the relative differences characterising the mass fluxes for $2 \cdot 10^{-6}$ m, $5 \cdot 10^{-6}$ m, $1 \cdot 10^{-5}$ m and $2 \cdot 10^{-5}$ m roughness heights, respectively. The relative difference results from a comparison of the mass flux for a given roughness height to the mass flux for a reference height without roughness. The final row of Table 3 contains the average relative difference for a given roughness height. Noticeably, with increasing roughness height, the mass

flux decreases. The only notable values of the relative difference were observed at OP3 and OP4. For these cases, the relative difference for all the roughness heights was approximately 3 and 5% for OP3 and OP4, respectively. The rest of the results were less significant and the highest average relative difference was equal to 2%. Ultimately, the overall influence on the results is insignificant. In spite of this, the case with the highest impact on MFR was chosen for all the future calculations, i.e., the case where the highest roughness was equal to $2 \cdot 10^{-5}$ m.

Table 3: Effect of roughness height influence on MFR.

Roughness height, m	$2 \cdot 10^{-6}$	$5 \cdot 10^{-6}$	$1 \cdot 10^{-5}$	$2 \cdot 10^{-5}$
OP		$\delta_{\dot{g}}$, %		
1	0.531	0.355	0.047	-0.277
2	0.442	0.209	-0.075	-0.460
3	-2.201	-2.674	-2.943	-3.209
4	-4.843	-5.145	-5.376	-5.597
5	-0.096	-0.514	-0.812	-1.288
6	-0.567	-0.896	-1.190	-1.507
7	-0.733	-1.012	-1.305	-1.663
Average, %:	1.345	1.544	1.678	2.000

4. Computational procedure

4.1. Solver settings

All numerical computations were performed using the ANSYS Fluent solver (ANSYS, Inc., 2011) under steady state conditions. The solver type was set as pressure-based and the solution method was pseudo-transient. The *Under-Relaxation Factors* for pressure and momentum were set to 0.25, and the turbulent kinetic energy and turbulent dissipation rate were set to 0.75, and the density, body forces, turbulent viscosity and specific enthalpy (UDS) were all set to 1 and, finally, the instantaneous vapour quality (UDS) was 0.04. The spatial discretisation for the pressure was set to the second order, whilst the power law was used for the turbulent kinetic energy, the turbulent dissipation rate and the specific enthalpy. For all the remaining variables, a second-order upwind was chosen. Convergence criteria were assumed to be the mass flow rate imbalance between the inlet and the outlet lower than 1% and the residual of all equations below 0.0001. For the HRM calculations, some HRM parameters caused a divergence of the computational process. The most significant problem with convergence was seen with OP8. The calculations did not diverge. No matter what HRM parameters or solver settings were chosen, the mass imbalance remained at an unacceptable level. The effect of minimum values of the absolute pressure on the cell facets of the numerical grid during iterations was monitored. The minimum facet values for cases that did not converge were oscillating greatly. The values of down peaks were negative, which is a non-physical feature of absolute pressure. As a result of this there are no results for OP8 presented in Table 3.

4.2. Mesh independence study

Mesh independence analysis was completed using OP1 in order to choose an appropriate mesh. Mass flux and throat pressure were the main analysis criteria used. The throat pressure is a parameter that directly influences the mass flux and must therefore be included in the mesh independence analysis. Correctly calculating the mass flux is the purpose of this study, so it was necessary to ensure that it was independent from the mesh density. In Tables 4 and 5, the results of the mesh independence analysis for HEM and HRM are presented, respectively. In the columns, the following quantities are presented: the mesh number, the number of mesh cells, the mass flux, the mass flux relative difference, the throat pressure, the throat pressure relative difference and the computational time. The relative difference for a given j-quantity is defined in Eq. (17).

$$\delta_j = \frac{j_i - j_{i-1}}{j_{i-1}} \tag{17}$$

where δ_j is the relative error corresponding to the j-quantity investigated, e.g., the mass flux. The subscript i denotes the mesh number being investigated.

For both HEM and HRM analyses, the maximum relative difference for the mass flux is lower than 1% and for the throat pressure 0.5%. The low values of the relative differences suggest a low sensitivity of the investigated quantities to the number of cells. However, a change in the relative difference with an increasing number of mesh cells is not asymptotic. It can be observed, in an increase of the relative difference for the mass fluxes between mesh no. 3 and 4 for the HEM analysis. To reach an asymptotic region, the relative difference must always decrease along with an increase in the number of cells. This decrease should, for increasingly refined meshes, gradually become more and more insignificant. This means that the Grid Convergence Index (GCI) procedure cannot be conducted for meshes investigated in this study. The asymptotic region is likely to be obtained for meshes with a higher number of cells, which is impractical from the perspective of the scope of this work. Nonetheless, the results are highly insensitive to the number of cells. Thus, mesh no. 3, which consists of almost 51 thousand quadrilateral cells, was chosen for all the calculations as a compromise between mesh independent results, physical field results, and computational time.

Table 4: Mesh analysis results for HEM.

No.	N, -	$\dot{g}$, kg s^{-1}m^{-2}	$\delta_{\dot{g}}$, %	p_{th}, Pa	δ_p, %	time
1	12,232	18,068	-	1,756,891	-	2 h 27 min
2	24,992	18,108	0.218	1,757,800	0.052	2 h 37 min
3	50,687	18,134	0.143	1,757,815	0.001	3 h 03 min
4	101,774	18,193	0.328	1,759,005	0.068	3 h 53 min
5	205,221	18,216	0.128	1,756,914	-0.119	6 h 18 min
6	412,166	18,218	0.011	1,752,980	-0.224	13 h 18 min

5. HRM modification

The HRM parameters were derived by Downar-Zapolski et al. (1996) where the Moby Dick experiments were used as the basis of the derivation. Thus, the original HRM parameters are, in

Table 5: Mesh analysis results for HRM.

No.	N, -	$\dot{g}$, kg s^{-1}m^{-2}	$\delta_{\dot{g}}$, %	p_{th}, Pa	δ_p, %	time
1	12,232	34,035	-	1,261,199	-	0 h 48 min
2	24,992	34,237	0.596	1,258,036	-0.251	0 h 52 min
3	50,687	34,242	0.012	1,257,902	-0.011	1 h 03 min
4	101,774	34,570	0.958	1,260,598	0.214	1 h 24 min
5	205,221	34,776	0.596	1,266,479	0.467	2 h 46 min
6	412,166	34,973	0.568	1,268,842	0.187	7 h 03 min

fact, empirical parameters applicable to a two-phase water flow simulation. There has previously been an attempt, mentioned in Section 3.2, to adapt these parameters to other fluids. Angielczyk et al. (2010) not only changed the definition of the non-dimensional pressure difference but also adjusted the value of the reference relaxation time from the original value of $3.84 \cdot 10^{-7}$ s derived by Downar-Zapolski et al. (1996) to $2.14 \cdot 10^{-7}$ s. This was completed in order to lower the discrepancy between the experimental data and the results of the calculations for CO_2 flow through an ejector that employed the HRM approach. In the previously mentioned work of Haida et al. (2018), complex procedures such as the GA were employed to change the HRM parameters and find optimal ones which provide the lowest discrepancy between computational and experimental data. The HRM parameters obtained provided the motive nozzle MFR for pressures below the critical point with an average relative difference lowered by 5.8 percentage points when compared to the average relative difference provided by Angielczyk et al. (2010) HRM parameters.

In recent work, an approach similar to the one used by Haida et al. (2018) was adopted. The HRM parameters were optimised using the same GA. This GA was also described and successfully used in the works concerning an ejector shape optimisation reported by Palacz et al. (2016, 2017b). The GA has the following parameters: the probability of uniform crossover, mutations and creep mutations set to 50%, 2% and 4%, respectively. The elitism option was used and the number of genes was set to 9. An individual gene consisted of three chromosomes i.e. these were the arguments of an objective function, OF. These arguments were the empirical constants defining the relaxation time in Eq. (9). The OF was defined according to Eq. (18).

$$OF\,(\theta_0,\ a,\ b) = \frac{1}{n}\sum_{i=1}^{n}\left|\frac{\dot{m}_{cal,\,i} - \dot{m}_{exp,\,i}}{\dot{m}_{exp,\,i}}\right| \tag{18}$$

The subscripts exp and cal denote the experimental and computational results, respectively. This is an average value of n relative differences. In the first optimisation configuration (C1), four OPs were chosen: OP1, OP3, OP5 and OP6. The population consisted of 6 individuals. In the second optimisation configuration (C2), all OPs except OP8 were chosen and the population consisted of 20 individuals.

To define the search range for each chromosome, an investigation into the HRM parameters was carried out. The investigation utilised Eq. (9) which is proposed for water at relatively high pressures. The main aim was to examine the influence of the reference relaxation time θ_0 and exponents a and b on the OF over broad ranges to find the general positions of the minima and

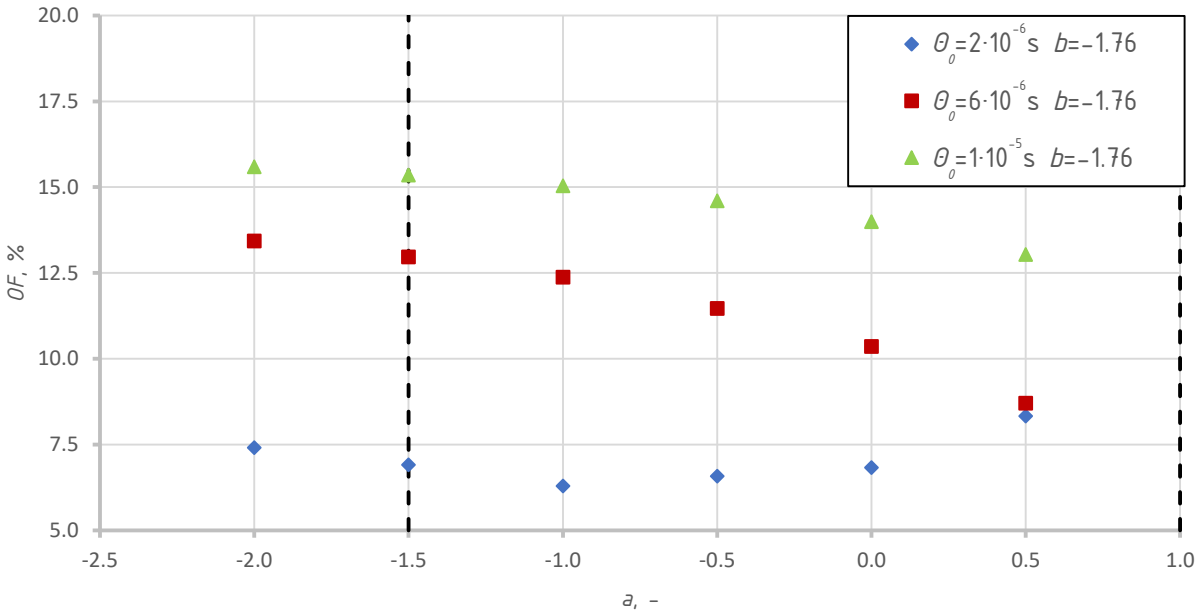

Figure 7: The influence of the exponent a on the OF value.

to define narrower search ranges around them. The influence of a on the OF can be seen in Fig. 7, whilst the influence of b on OF is given in Fig. 8, for three values of θ_0. When examining the influence of a, the value of b was chosen according to Downar-Zapolski et al. (1996). The exponent b was examined in a similar manner.

The upper limits of the broad ranges were limited by the convergence of calculations, while the lower limits resulting from decreasing values of exponents provided increasing values of OF. The dashed, vertical lines represent the defined narrow ranges of the search around the minima. The lower limits of the search ranges were set to capture the minimum associated with $\theta_0 = 2 \cdot 10^{-6}$ s. The upper boundary of the search ranges were set with the same parameters as the broad ranges. Moreover, at the upper boundary, the minimum could be closer to the central value of the reference relaxation time $\theta_0 = 6 \cdot 10^{-6}$ s, especially in the case of the b exponent. Thus, the search range for θ_0 was chosen from $2 \cdot 10^{-6}$ s to $6 \cdot 10^{-6}$ s. For the exponents, the search range for a was chosen from -1.5 to 1.0 and for b from -2.5 to -0.9.

The optimised HRM parameters together with the obtained OF minima are presented in Table 6. For C1, the optimisation procedure was set to 30 generations, although the minimum OF value was already reached after the 19$^{\text{th}}$ generation. The minimum OF for C2 presented in the table was achieved by the 12$^{\text{th}}$ generation. The minimum OF for C1 and C2 are highlighted in bold font. The seven OPs were taken into account for OF_{C2}, which gives a better representation of the final result. However, OF_{C2} had an insignificantly better final result (5.27%<5.28%) than OF_{C1}. The relative difference for the rest of the OPs and a detailed description of the results are presented in Section 6.2.

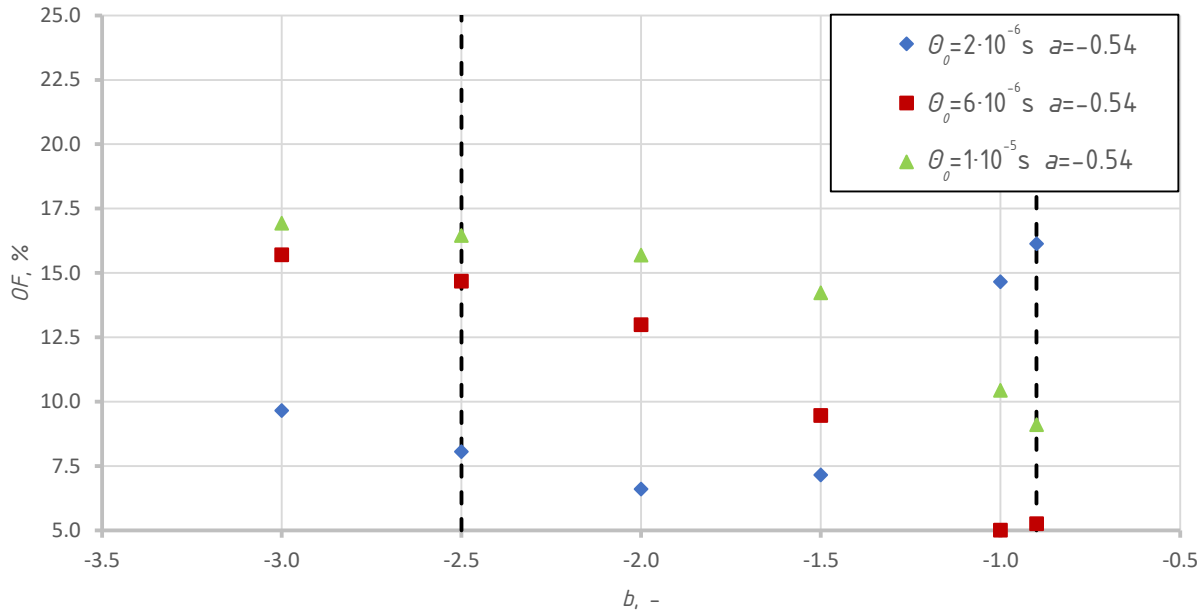

Figure 8: The influence of the exponent b on the OF value.

Table 6: The optimised HRM parameters.

	OF_{C1}, %	OF_{C2}, %	θ_0, s	a, -	b, -
C1:	**4.92**	5.28	$4.98 \cdot 10^{-6}$	-0.587	-1.100
C2:	4.87	**5.27**	$5.64 \cdot 10^{-6}$	-0.687	-0.968

6. Results and discussion

6.1. HEM results

The relative differences (denoted as δ) for the mass flow rate calculated using the HEM model are presented in Table 7. The relative differences are defined in accordance with Eq. (17) and for this case the subscripts i and $i-1$ denote the calculated and experimental MFR, respectively. Similarly, the subscripts are used in Eq. (18) for defining the OF. The second and third columns contain the HEM results and the relative differences, respectively. The next two columns contain the numerical results from HEM vs the Bernoulli equation. In the sixth column, the saturation pressure is given. The last two columns contain the mass flux resulting from an isentropic expansion, defined in Eq. (19), and the relative difference δ_{s_o}, between the Bernoulli and isentropic mass fluxes. Eq (19) is defined

$$\dot{m} = C_f A_{th} \rho\left(p_{sat},\ s_o\right) \sqrt{2\left[E - h\left(p_{sat},\ s_o\right)\right]} \tag{19}$$

where $\rho\left(p_{sat},\ s_o\right)$ is the density and $h\left(p_{sat},\ s_o\right)$ is the specific enthalpy, which are both at the throat. The root denotes the velocity resulting from the energy conservation for the adiabatic flow

with no work done. The discharge coefficient C_f was assumed as given by Chen et al. (2009) as 0.94. The calculations were completed to investigate the influence of the potential density change. As can be seen, the highest relative difference is -0.13%. Hence, the influence due to the density change is negligible, as predicted.

The average relative difference obtained using the HEM formula was 42.25%. This result is unsatisfactory, however not unexpected. As predicted in Section 1, the flow choked on the saturation pressure resulting in a significant underestimation of the MFR. The expansion process of the still incompressible liquid, starting from operating points in the sub-cooled region, was unrestricted due to the tremendously high sonic velocity in the liquid region. This allows the liquid to achieve a velocity higher than the low sonic velocity of the two-phase region before reaching the saturation line. The saturation line is the place where a severe HEM sonic velocity discontinuity occurs. The liquid, which is still accelerating, reaches the saturation line where, due to the presence of a discontinuity, the sonic velocity drops below the flow velocity. This results in an abrupt transition from subsonic to supersonic flow and immediate choking as shown by Downar-Zapolski et al. (1996). With the assumption of the infinite rate of heat and mass transfer, the throat pressure cannot be lower than the saturation pressure which results in relatively low flow velocities and, thus, low MFRs.

The expansion process between the OP conditions and the saturation pressure concerns only the liquid. Thus the choked MFR resulting from the HEM approach should be easily calculated from the Bernoulli equation (Eq. (1)); this was mentioned in the earlier reference to Städtke. To confirm this, the results from Eq. (1) and the relative differences between the HEM calculations are presented in the fourth and fifth columns of Table 7. The average relative difference is 4.95%. For the last three points, the mass flow rates obtained, based on Eq. (1), significantly exceeded those from HEM. This is due to the fact that the Bernoulli equation provides 1-D results, while the CFD calculation provides 2-D results, presented in Fig. 9 and described in more detail in the next paragraph.

Table 7: HEM mass fluxes and relative differences.

OP	$\dot{g}_{HEM}$ kg s^{-1}m^{-2}	δ_{HEM} %	$\dot{g}_{bern}$ kg s^{-1}m^{-2}	δ_{bern} %	p_{sat} Pa	$\dot{g}_{s_o}$ kg s^{-1}m^{-2}	δ_{s_o} %
1	18,134	-41.42	18,319	1.02	1,783,824	18,305	-0.08
2	18,182	-44.04	18,429	1.36	1,781,959	18,415	-0.08
3	17,820	-48.09	17,644	-0.99	1,794,105	17,632	-0.07
4	17,788	-50.96	17,568	-1.24	1,797,386	17,556	-0.07
5	17,501	-53.96	16,872	-3.59	1,810,554	16,861	-0.07
6	20,731	-40.44	22,560	8.83	1,690,588	22,536	-0.11
7	23,160	-33.21	25,745	11.16	1,611,841	25,712	-0.13
8	23,401	-25.87	26,074	11.42	1,606,663	26,040	-0.13
Average:	-	42.25	-	4.95	-	-	0.09

The relative differences between the CFD and Bernoulli equation results are small enough to conclude that choking takes place at the saturation line. Therefore, the underestimated HEM mass flow rates result from the assumptions of the HEM model. The evaporation front expressed by the

saturation pressure isobar is presented in Fig. 9. The lower limit of the pressure field indicates the isobaric saturation pressure profiles for selected OPs. The colour maps of the pressure range are separate for each profile. This is necessary since the lowest value of the range must be the saturation pressure appropriate for each OP. The upper value of the range is the inlet pressure. The order of the OPs starts from the profiles with the shape closest to a straight line. For a low difference between the inlet and the saturation pressure, the profile of the saturation pressure at the throat is close to a straight line (representing the choking plane) corresponding to the 1-D approach of the Bernoulli equation. With an increasing difference between the inlet and the saturation pressure, the saturation pressure profile loses its similarity to a straight line and tends towards a quasi-parabolic shape. Thus, higher pressure than the saturation pressure can be found at the choking plane.

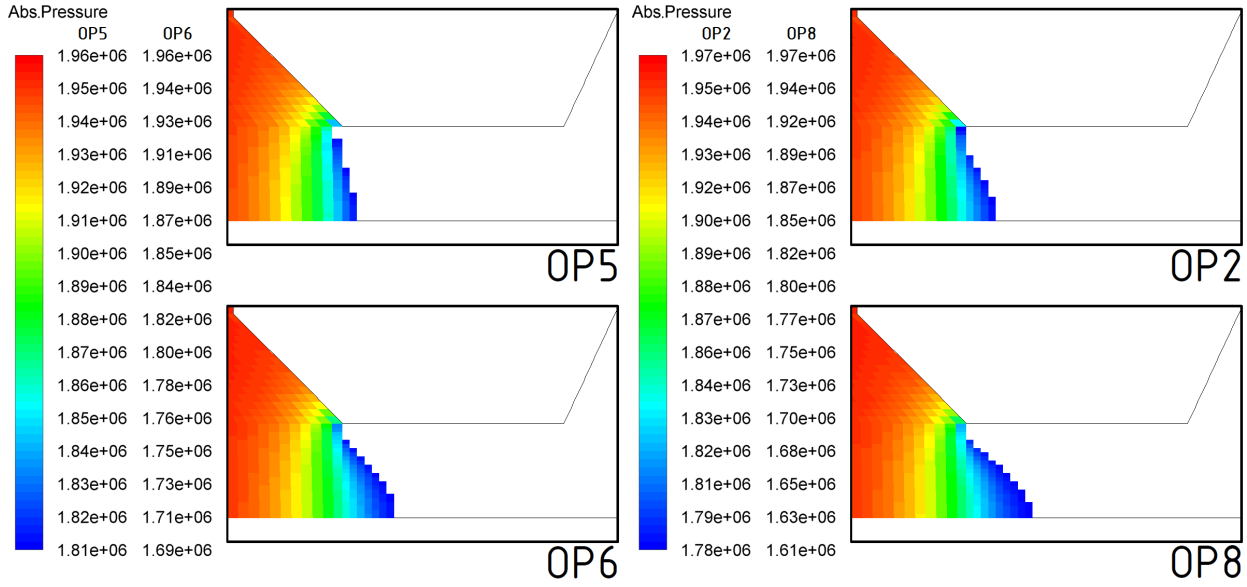

Figure 9: The lower limit of the pressure field results, indicating isobaric profiles for the saturation pressure inside the valve throat for various OPs.

Finally, one can conclude that the HEM model is, at the very least, inadequate for the conditions examined. Further description of the HEM results will be given while comparing the HEM results with the HRM results in Section 6.2.

6.2. HRM results

In this section, five variants of the HRM parameters acquired from the literature and the optimisation procedure are addressed. Table 8 contains all of the parameter variants and their definitions:

- *Variant 1*: the Low-pressure variant which refers to the Downar-Zapolski et al. (1996) HRM parameters characterised in Eq. (7).
- *Variant 2*: the High-pressure variant which refers to the Downar-Zapolski et al. (1996) HRM parameters characterised in Eq. (9).
- *Variant 3*: custom parameter calculations (CPC) variant containing $\theta_0 = 3.84 \cdot 10^{-6}$ s.

- *Variant 4*: C1 variant which is a result of CPC parameter optimisation using only four OPs.
- *Variant 5*: C2 variant which is a result of CPC parameter optimisation using seven OPs.

Haida et al. (2018) performed a parametrisation procedure of each relaxation time constant in the R744 two-phase ejector to evaluate an influence of θ_0, a exponent, and b exponent on the metastable flow behaviour. The authors stated that the most significant parameter that caused a delay in the flow evaporation during flashing process was θ_0. Therefore, θ_0 defined for Variant 1 for low-pressure fluid was much higher when compared to Variant 2 for high-pressure fluid due to the different relaxation time value at the specified pressure ranges. Furthermore, an increase of θ_0 accelerated the flashed flow during expansion in the two-phase region near saturation liquid. A decrease of the a exponent described the void fraction that caused higher impact of the local void fraction on the relaxation time. According to Haida et al. (2018), an increase of a exponent caused an increase of the pressure gradient in the two-phase metastable region near the saturation liquid. The influence of the non-dimensional pressure ratio has a higher impact when the flow is expanded near the critical point (Haida et al., 2018). Furthermore, an increase of the b exponent affected the pressure gradient decrease in the two-phase region near the saturation liquid.

Table 8: HRM parameter variants.

Variant	Name	θ_0, s	a, -	b, -
1	Low-pressure	$6.51 \cdot 10^{-4}$	-0.257	-2.240
2	High-pressure	$3.84 \cdot 10^{-7}$	-0.540	-1.760
3	CPC	$3.84 \cdot 10^{-6}$	-0.540	-1.760
4	C1	$4.98 \cdot 10^{-6}$	-0.587	-1.100
5	C2	$5.64 \cdot 10^{-6}$	-0.687	-0.968

The calculations for Variant 1 of OPs 5 and 8 did not reach a final convergence. The rest of the OPs resulted in overestimated MFRs and the average relative difference is 17.38%. The calculations for Variant 2 resulted in underestimated MFRs which are expected at low values of θ_0. The average relative difference for OPs from 1 to 4 is 26.44%. The OPs from 5 to 8 did not achieve the assumed maximum mass imbalance, which is similar to the convergence problems described at the end of Section 3.5. A longer relaxation time should result in a higher MFR, therefore the value of $\theta_0 = 3.84 \cdot 10^{-7}$ s from Variant 2 was arbitrarily multiplied by 10 to positively affect the relative differences. Using a new value of $\theta_0 = 3.84 \cdot 10^{-6}$ s assigned as Variant 3, the results were in surprisingly good agreement with the experimental results. Only OP8, as mentioned in Section 3.5 above, did not reach the assumed maximum mass imbalance. Therefore, all further discussions will consider OPs from 1 to 7. The average relative difference for OPs from 1 to 7 was 8.18%. The case for a relatively broad range of the HRM parameters converged. This fact means that Variant 3 is suitable for optimisation and will be used in further calculations.

In Fig. 10, the relative differences are shown for the HRM calculations. Average relative differences of 8.18%, 5.28% and 5.27% were obtained for Variant 3, Variant 4 and Variant 5, respectively. As discussed in Section 1, the sub-cooled liquids expanding through nozzles into the two-phase region are influenced by thermodynamic non-equilibrium, as confirmed by satisfactory

agreement with experimental results. The metastability presence allows for a deeper decompression of the superheated liquid, which remains at high density. This, in turn, results in high MFRs in comparison to HEM and hence the lower values of the relative differences for the optimised HRM parameters. Although, for OP5, both optimised HRM calculations underestimated the measured mass flow rate, which resulted in a higher relative difference.

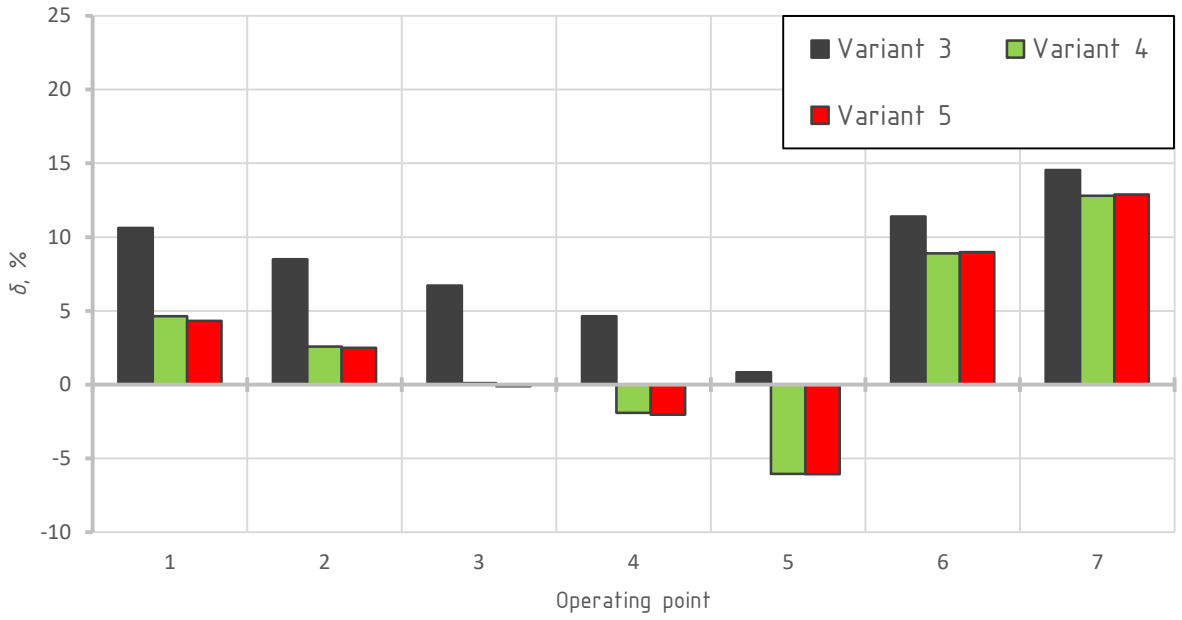

Figure 10: The relative differences between the experimental and the HRM mass flow rate for Variants 3-5.

The axial distribution of the pressure and velocity along the EEV for OP1 was compared between Variant 4 and 5. The average relative differences are 0.05% and 0.28% for the pressure and velocity, respectively. These values confirm that the difference between Variants 4 and 5 is negligible. Hereinafter, all the results concerning the HRM are represented by the results from Variant 5 because the lowest discrepancy is found between them and the measurement data.

The reference relaxation times and pressures at the inlet of the main nozzles of the expansion devices are compared for the current study and data available in the literature, see Table 9. Since HRM parameters for R410A cannot be found in the literature, the examples in Table 9 used CO_2. The general trend, although not monotonic, is that lower pressure corresponds to a higher reference relaxation time.

The field results of the pressure and the density for HEM and HRM are shown in Fig. 11 and Fig. 12, respectively. These results were obtained for OP1. The pressure fields for HEM show that the pressure at the throat and the constant CS channel is near the saturation pressure (1,783,824 Pa for OP1, see Table 7). This is consistent with the discussion above with regard to the HEM and Bernoulli equation results, indicating that choking takes place at the saturation line. In the HEM density field, a significant drop can be seen at the saturation pressure profile location; the location presented in Fig. 9. These low-density values characterise the isentropic expansion for

Table 9: Reference relaxation time comparison.

Source of data	p_{in}, bar	p_{in}/p_c, %	θ_0, s
Angielczyk et al. (2010)	91.00	123	$2.00 \cdot 10^{-7}$
Haida et al. (2018)	≥73.77	≥100	$1.00 \cdot 10^{-7}$
	⟨59.00, 73.77)	⟨80, 100)	$9.00 \cdot 10^{-6}$
	<59.00	<80	$1.50 \cdot 10^{-6}$
Current study	19.64	27	$4.98 \cdot 10^{-6}$
	19.64	27	$5.64 \cdot 10^{-6}$

pressures lower than the saturation pressure because of the thermodynamic equilibrium assumption. The pressure values for HRM are much lower than those for HEM. In the throat, the pressure is approximately 1,300,000 Pa. Despite such a low-pressure value and the fact that the expansion entered the two-phase region, the density remains at 1,046 kg/m^3, which is a typical value for the liquid. The HRM density field result visualises the superheated, metastable liquid presence at pressures at which thermodynamic equilibrium provide much lower density values. The thermodynamic non-equilibrium effect is observable in the throat and can also be confirmed using the real fluid EoS, which in the following example were the REFPROP property functions. For OP1, the inlet specific entropy $s_o = 1,151$ J/(kg · K) and the aforementioned pressure $p = 1,300,000$ Pa resulted in a density of ~382 kg/m^3, not 1,046 kg/m^3, which can be seen in the HRM density field results. The observable thermodynamic non-equilibrium effects, captured by the HRM approach, gave higher MFRs than HEM.

The axial density distribution along the EEV is shown in Fig. 13 and Fig. 14. The quantity defining the abscissa is a dimensionless length. It is determined by dividing the actual position along the EEV, l, by the total length of the EEV, l_o. Fig. 13 shows the HEM density and REFPROP density $\rho = f(p,\ s_o)$ where the pressure p is changing along the EEV and the parameter s_o is the inlet specific entropy. HEM assumes thermodynamic equilibrium which means that all the parameters are in agreement with a real fluid EoS, whether it is a pressure enthalpy chart or REFPROP equations. However, the discrepancy may be observable inside the abrupt diffuser. The expansion in the abrupt diffuser may no longer be treated as isentropic. In fact, this is the place where the entropy rise occurs, due to the lost potential of the high inlet pressure. For the same pressure, the density corresponding to s_o is higher than the density corresponding to the entropy which is higher than s_o. For instance, at location $l/l_o = 0.07$, where the pressure is 1,354,210 Pa, the entropy is equal to 1,154 J/(kg · K). For these parameters, the density is equal to 407.8 kg/m^3 which is lower than $\rho = f(p = 1,354,210 \text{ Pa},\ s_o = 1,151 \text{ J/(kg} \cdot \text{K)}) = 422.6$ kg/m^3.

Fig. 14 depicts the thermodynamic non-equilibrium effect for HRM. The density from the EoS reflects the pressure change along the EEV, while the HRM remains at a liquid density, despite the pressure decrease. The highest differences between HRM and the EoS density, which are approximately equal to 600 kg/m^3, also indicate the location of the most significant metastability. The metastability effect occurs suddenly in the middle of the nozzle and at $l/l_o = 0.065$ starts to fade.

Fig. 15 presents the field results for the velocity for HEM and HRM. The velocity before the abrupt diffuser for HEM is lower than the one for HRM, which is a result of depressurisation lim-

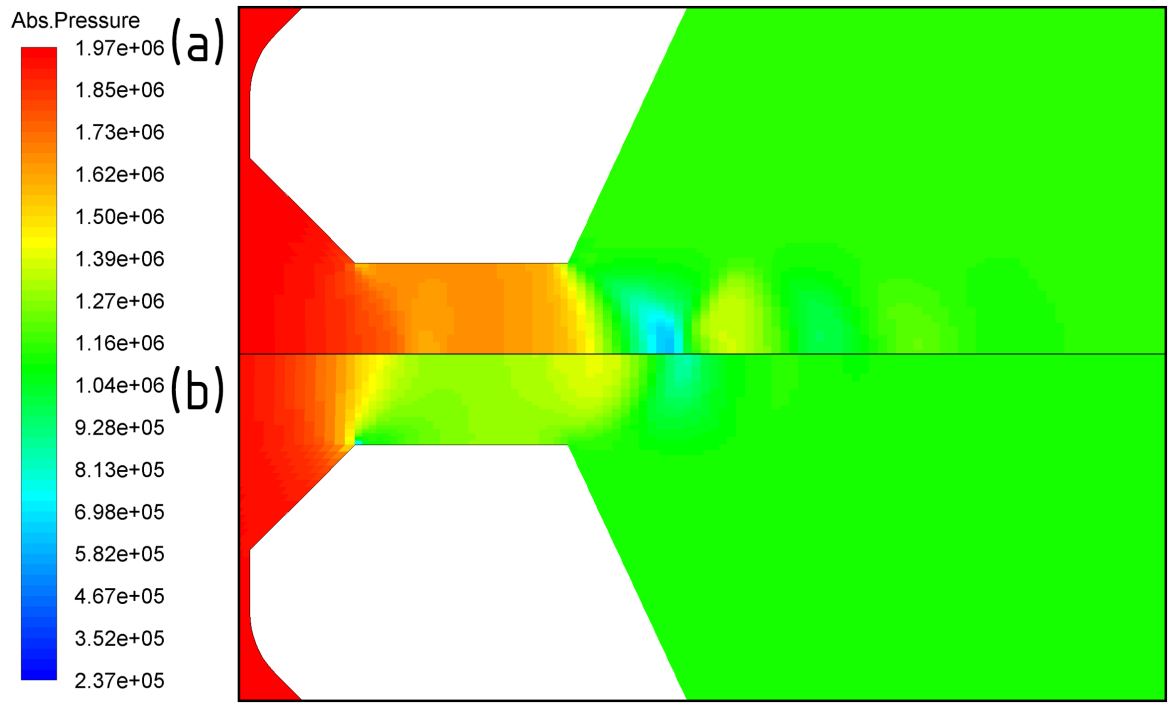

Figure 11: A comparison of the pressure in (Pa) for OP1 between (a) HEM and (b) HRM for Variant 5.

ited by the saturation pressure. Due to this fact, a higher pressure drop occurs in the abrupt diffuser which results in a higher HEM velocity near the shockwave by approximately 38 m/s compared to the HRM velocity. In addition, the HRM velocity increase associated with the shockwave occurs further downstream when compared to the location of the HEM velocity increase.

Fig. 16 presents the field results of the vapour mass fraction for HEM and HRM. For HEM, the fluid enters the two-phase region at the entrance of the constant CS channel and then, in the abrupt diffuser, the vapour mass fraction significantly increases to approximately 22.4% due to the significant pressure drop. For HRM, the constant CS channel is filled with the metastable liquid, thus the vapour mass fraction is 0%. Inside the abrupt diffuser, the vapour mass fraction increases due to the fact that the metastable liquid core is terminated by the shockwave.

7. Conclusions

Both HEM and HRM models were used in the CFD analysis of R410A refrigerant flow through an EEV. The HRM parameters were optimised to minimise the model's MFR discrepancies. The influence of the HRM parameters was investigated to define the search range for the optimisation procedure. The results of HEM and HRM calculations were compared with laboratory measurements. The HEM results were also compared to the analytical solution to show the agreement of the results with the model assumptions. The HRM outputs were compared with different HRM parameters to show the effect of the optimisation. The field results and graphs with an axial

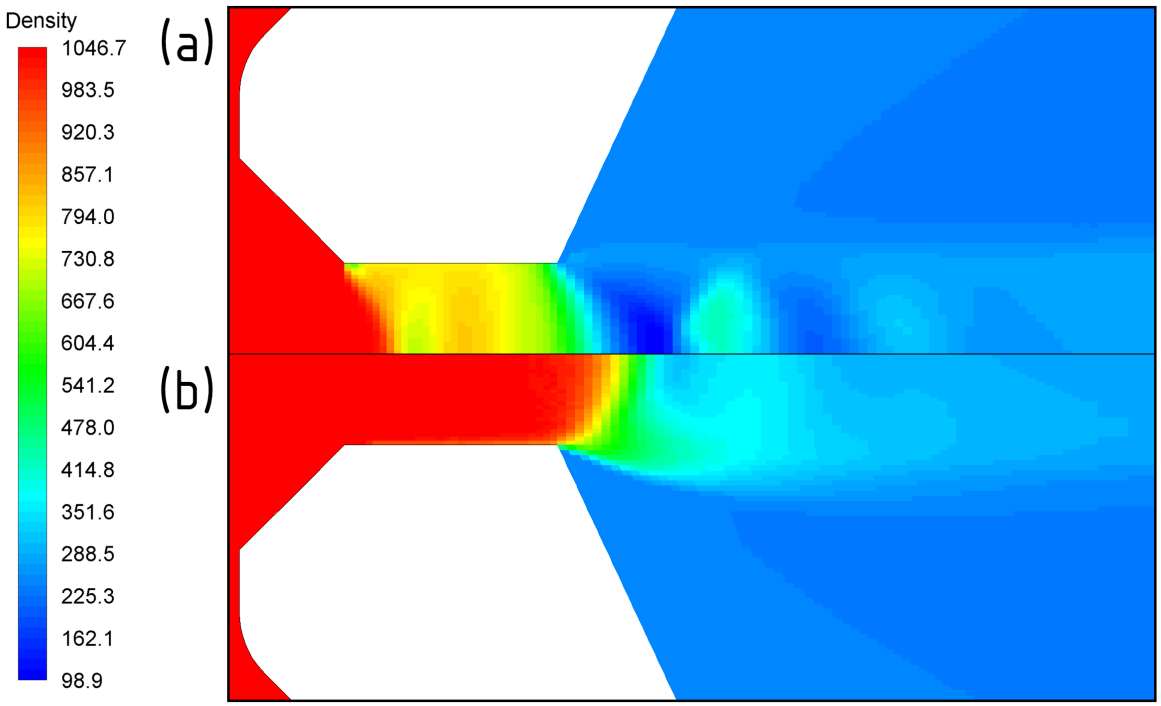

Figure 12: A comparison of the density in (kg/m^3) for OP1 between (a) HEM and (b) HRM for Variant 5.

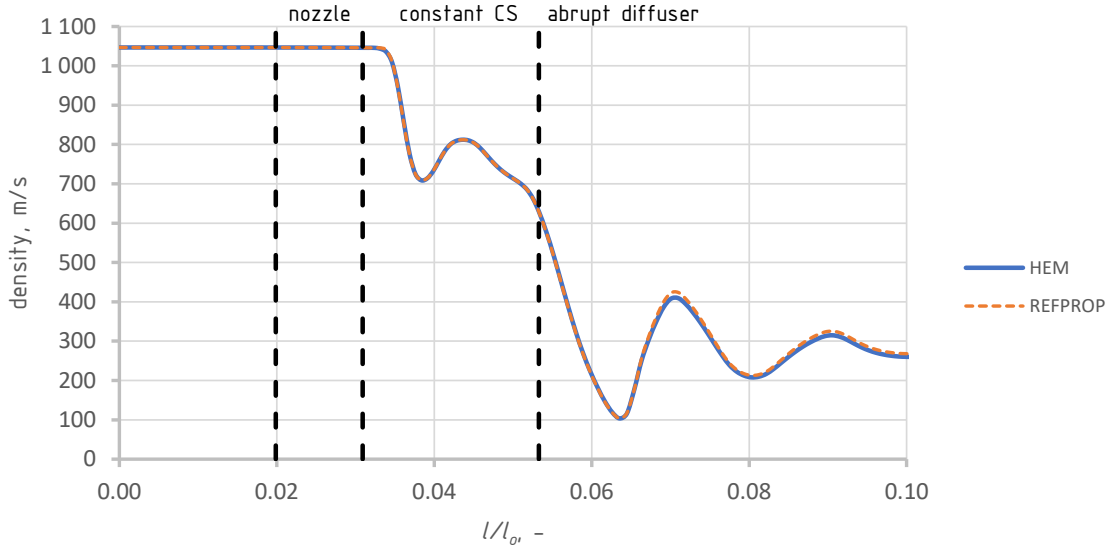

Figure 13: The axial distribution of the HEM and the REFPROP density.

distribution of parameters were presented to show the differences between the HEM and HRM approach.

The results for the HEM calculations significantly underestimated mass flow rates when compared to the measured results. The resulting average relative difference was 42%. This resulted

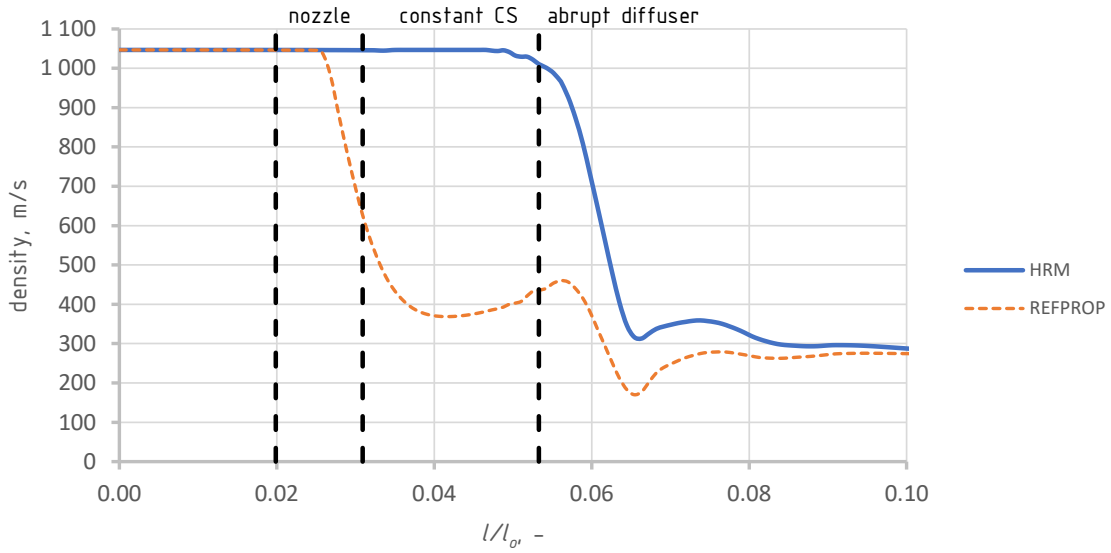

Figure 14: The axial distribution of the HRM for Variant 5 and the REFPROP density.

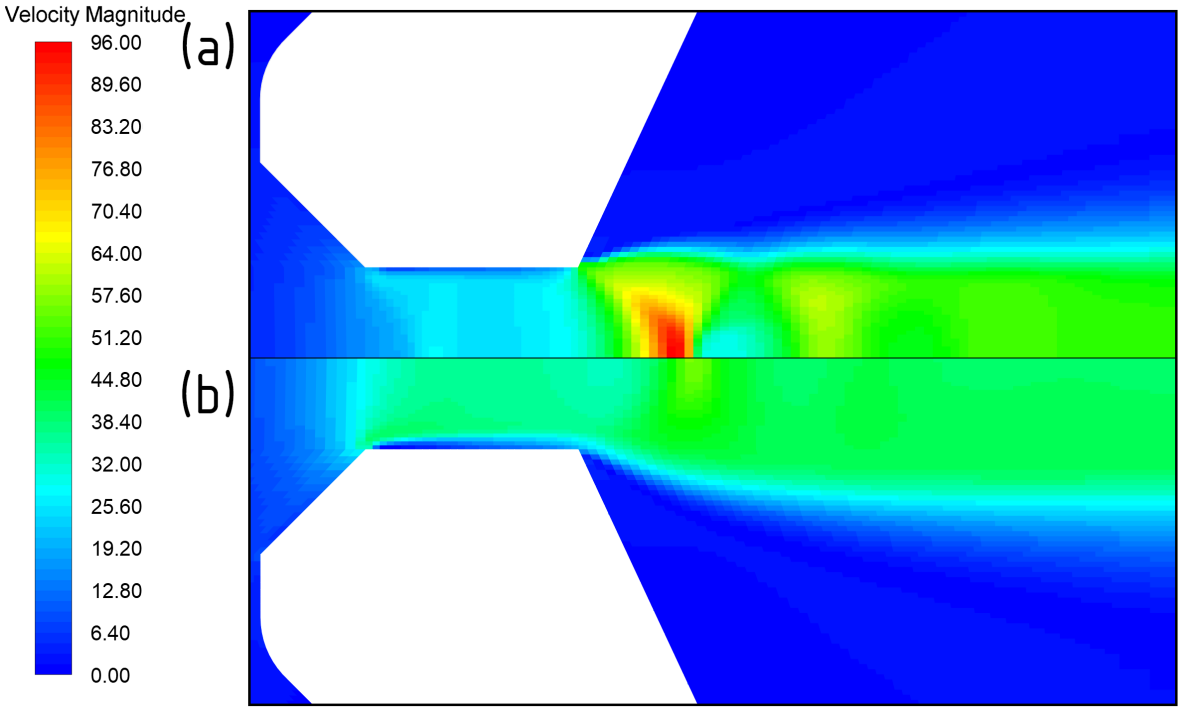

Figure 15: A comparison of the velocity in (m/s) for OP1 between (a) HEM and (b) HRM for Variant 5.

from the model limitations and its inability to address the sonic velocity values for the two-phase region near the liquid saturation line. This conclusion was confirmed by comparing the HEM results with analytical ones and the average difference was below 5% which is satisfactorily low. Thus, the flow for the conditions that were used, cannot be modelled using HEM because the

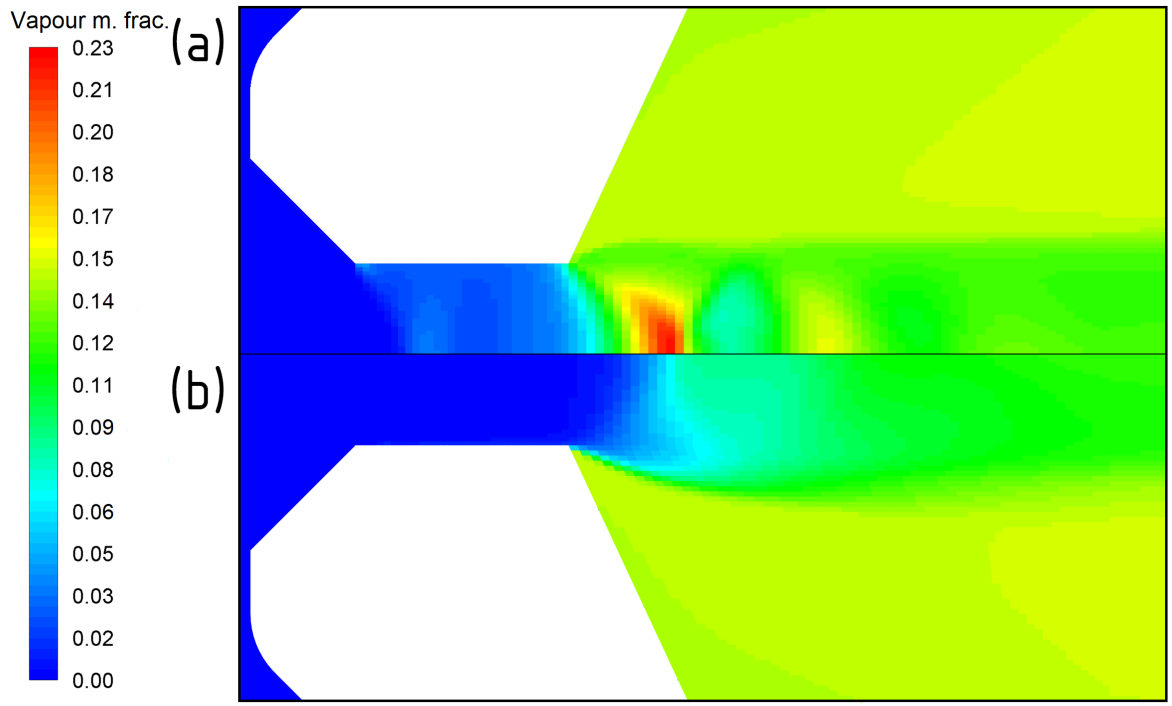

Figure 16: A comparison of the vapour mass fraction for OP1 between (a) HEM and (b) HRM for Variant 5.

thermodynamic non-equilibrium effects are too significant.

The results for HRM using water parameters from the literature, provided results with relative differences of approximately 17% for the low-pressure equation parameters and 26% for the high-pressure equation parameters. The large underestimation of the MFR using the parameters of the high-pressure equation is due to the low reference relaxation time. As the higher MFR corresponds to the higher relaxation time, the reference relaxation time parameter, which was ten times higher, provided a lowered average relative difference of 8.2%. Finally, for the optimised HRM parameters, the average relative difference was approximately 5.3%. While the optimised HRM parameters determined in this study apply only to the fluid, geometry and conditions used, the methodology, which gives those parameters, can be applied to different geometries and fluids since it was successfully applied in this study and the Haida et al. (2018) study which investigated CO_2 flow through the ejector. This gives researchers the potential to adapt the HRM approach to different working fluids and this can be highly desirable for environmental reasons, e.g., HFO or natural refrigerants. Combining this with the fact that HRM can be used for different expansion devices, like an ejector, a modified HRM may be an attractive approach for modelling novel solutions in refrigeration from an environmental perspective. Furthermore, this is the first application of the modified HRM to an EEV simulation and the first introduction of the HRM parameters for R410, while in the literature, the HRM parameters are only available for water and CO2. In addition, the model developed can serve as a design optimisation tool for the high efficiency EEV types examined in the current study and can be useful for other types of valves such as a needle-using

EEV. The model design and optimisation capabilities will be increased even more in the future, when a tool based on entropy generation will be implemented for the model, taking advantage of CFD modelling ability to show local phenomena.

Acknowledgements

The work of Jacek Smolka and Michal Haida was partially supported by the statutory research fund of the Silesian University of Technology, Gliwice, Poland. In addition, Michal Haida would like to acknowledge partial support from the “START” scholarship funded by FNP.

Nomenclature

Acronyms and abbreviations

ANN	artificial neural network
CFD	Computational Fluid Dynamics
COP	coefficient of performance
CS	cross-section
DEM	Delayed Equilibrium Model
EEV	electronic expansion valve
EoS	equation of state
EV	expansion valve
GA	genetic algorithm
GCI	Grid Convergence Index
HEM	Homogeneous Equilibrium Model
HRM	Homogeneous Relaxation Model
MFR	mass flow rate
OC	optimisation configuration
OF	objective function
OP	operating point
UDS	User-Defined Scalar

Latin letters

A	area, m^2
A_{th}	cross-section area of the throat, m^2
a	exponent of the void fraction, -
b	exponent of the non-dimensional pressure difference, -
C_1	turbulence model coefficient, -
$C_{1\epsilon}$	turbulence model coefficient, -
C_2	turbulence model coefficient, -
$C_{3\epsilon}$	turbulence model coefficient, -
C_f	discharge coefficient for incompressible liquid, -
c_p	specific heat capacity, J $kg^{-1}K^{-1}$
E	total specific enthalpy, J kg^{-1}
$\dot{g}$	mass flux, kg $s^{-1}m^{-2}$
G_b	generation of k due to buoyancy, kg $s^{-3}m^{-1}$
G_k	generation of k due to mean velocity gradients, kg $s^{-3}m^{-1}$
h	specific enthalpy, J kg^{-1}
j	quantity compared in the relative difference, -
k	turbulent kinetic energy, m^2 s^{-2}
l	length, m
l_o	total length, m
$\dot{m}$	mass flow rate, kg s^{-1}
N	number of mesh cells, -
p	pressure, Pa
s	specific entropy, J $kg^{-1}K^{-1}$
S	mean strain rate magnitude, s^{-1}
$\boldsymbol{S_{ij}}$	mean rate-of-strain tensor, s^{-1}
T	temperature, K
t	time, s
$\boldsymbol{u}$	velocity vector, m s^{-1}
u	velocity vector component, m s^{-1}

u_x velocity vector component perpendicular to the gravitational vector, m s^{-1}
u_y velocity vector component parallel to the gravitational vector, m s^{-1}
x vapour mass fraction, -
Y_M fluctuating dilatation dissipation, kg $s^{-3}m^{-1}$

Greek Letters

α void fraction, -
Γ vapour generation rate, kg $m^{-3}s^{-1}$
δ relative difference, %
ϵ turbulent dissipation rate, m s^{-3}
η mean strain, -
θ relaxation time, s
θ_0 reference relaxation time, s
κ heat capacity ratio, -
λ thermal conductivity, W $m^{-1}K^{-1}$
μ dynamic viscosity, kg $m^{-1}s^{-1}$
μ_{turb} turbulent viscosity, kg $m^{-1}s^{-1}$
ν kinematic viscosity, m^2 s^{-1}
ρ density, kg m^{-3}
σ_ϵ turbulent Prandtl number for the turbulent dissipation rate, -
σ_k turbulent Prandtl number for the turbulent kinetic energy rate, -
$\boldsymbol{\tau}$ stress tensor, Pa
ϕ non-dimensional pressure difference at the relatively high pressure, -
ψ non-dimensional pressure differenceat the relatively low pressure, -

Subscripts

bern Bernoulli
c thermodynamic critical point
cal calculations
*C*1 optimisation configuration 1
*C*2 optimisation configuration 2
CPC custom parameter calculations
eq equilibrium
exp experimental
hp high-pressure
in inlet
l liquid saturation line
lp low-pressure
min minimal
ml metastable conditions
o stagnation
out outlet
s saturation
th throat
turb turbulent
v vapour saturation line

References

Anderson, J., 1995. Computational Fluid Dynamics: The Basics with Applications. McGraw-Hill.

Angielczyk, W., Bartosiewicz, Y., Butrymowicz, D., Seynhaeve, J.M., 2010. 1-D modeling of supersonic carbon dioxide two-phase flow through ejector motive nozzle. International Refrigeration and Air Conditioning Conference, Purdue e-Pubs, Purdue University .

ANSYS, Inc., 2011. ANSYS Fluent User's Guide. Canonsburg, PA.

Attou, A., Seynhaeve, J., 1999a. Steady-state critical two-phase flashing flow with possible multiple choking phenomenon: Part 1: Physical modelling and numerical procedure. Journal of Loss Prevention in the Process Industries 12, 335 – 345.

Attou, A., Seynhaeve, J., 1999b. Steady-state critical two-phase flashing flow with possible multiple choking phenomenon: Part 2: comparison with experimental results and physical interpretations. Journal of Loss Prevention in the Process Industries 12, 347 – 359.

Baek, S., Ko, S., Song, S., Ryu, S., 2018. Numerical study of high-speed two-phase ejector performance with R134A refrigerant. International Journal of Heat and Mass Transfer 126, 1071 – 1082.

Besagni, G., Inzoli, F., 2017. Computational fluid-dynamics modeling of supersonic ejectors: Screening of turbulence modeling approaches. Applied Thermal Engineering 117, 122 – 144.

Bilicki, Z., Kestin, J., 1990. Physical aspects of the relaxation model in two-phase flow. Proceedings of the Royal Society of London. Series A, Mathematical and Physical Sciences 428, 379–397.

Bodys, J., Smolka, J., Palacz, M., Haida, M., Banasiak, K., 2020. Non-equilibrium approach for the simulation of CO_2 expansion in two-phase ejector driven by subcritical motive pressure. International Journal of Refrigeration 114, 32 – 46.

Cao, X., Li, Z.Y., Shao, L.L., Zhang, C.L., 2016. Refrigerant flow through electronic expansion valve: Experiment and neural network modeling. Applied Thermal Engineering 92, 210–218.

Chen, L., Liu, J., Chen, J., Chen, Z., 2009. A new model of mass flow characteristics in electronic expansion valves considering metastability. International Journal of Thermal Sciences 48, 1235–1242.

Chen, T., Bae, K.J., Kwon, O.K., 2018. Empirical correlation development of R245FA flow in electronic expansion valves. International Journal of Refrigeration 88, 284–290.

Chen, T., Bae, K.J., Kwon, O.K., 2019. Mass flow rate prediction of R1233ZD through electronic expansion valves based on ANN and power-law correlation models. Applied Thermal Engineering 158, 113826.

Chen, T., Cha, D.A., Kwon, O.K., 2017. Experimental investigation on mass flow characteristics of R245FA through electronic expansion valve. Applied Thermal Engineering 125, 111 – 117.

Croquer, S., Poncet, S., Aidoun, Z., 2016. Turbulence modeling of a single-phase R134A supersonic ejector. part 1: Numerical benchmark. International Journal of Refrigeration 61, 140 – 152.

Downar-Zapolski, P., Bilicki, Z., Bolle, L., Franco, J., 1996. The non-equilibrium relaxation model for one-dimensional flashing liquid flow. International Journal of Multiphase Flow 22, 473–483.

Elias, E., Lellouche, G.S., 1994. Two-phase critical flow. International Journal of Multiphase Flow 20, 91–168.

Geng, L., Liu, H., Wei, X., 2019. CFD analysis of the flashing flow characteristics of subcritical refrigerant R134A through converging-diverging nozzles. International Journal of Thermal Sciences 137, 438–445.

Grønheden, E., 2015. Modelling non-equilibrium flashing flow using the homogeneous relaxation model for refrigeration valves. Aarhus School of Engineering.

Haida, M., Smolka, J., Hafner, A., Palacz, M., Banasiak, K., Nowak, A.J., 2018. Modified homogeneous relaxation model for the R744 trans-critical flow in a two-phase ejector. International Journal of Refrigeration 85, 314 – 333.

Henry, R.E., Grolmes, M.A., Fauske, H.K., 1971. Pressure-pulse propagation in two-phase one- and two-component mixtures. ANL-7792 Reactor Technology, United States.

Ingle, R., Rao, V.S., Mohan, L.S., Dai, Y., Chaudhry, G., 2015. Modelling of flashing in capillary tubes using homogeneous equilibrium approach. Procedia IUTAM 15, 286–292. IUTAM Symposium on Multiphase Flows with Phase Change: Challenges and Opportunities.

Kolev, N.I., 2015. Multiphase Flow Dynamics 5: Nuclear Thermal Hydraulics. Springer International Publishing.

Lahey, R.T., Moody, F.J., 1993. The thermal-hydraulics of a boiling water nuclear reactor. American Nuclear Society.

Lee, M.S., Lee, H., Hwang, Y., Radermacher, R., Jeong, H.M., 2016. Optimization of two-phase R600A ejector geometries using a non-equilibrium CFD model. Applied Thermal Engineering 109, 272 – 282.

Lemmon, E.W., Bell, I., Huber, M.L., McLinden, M.O., 2010. NIST Standard Reference Database 23: Reference Fluid Thermodynamic and Transport Properties-REFPROP, Version 9.0, National Institute of Standards and Technology.

Li, W., 2013. Simplified modeling analysis of mass flow characteristics in electronic expansion valve. Applied Thermal Engineering 53, 8 – 12.

Mazzelli, F., Little, A.B., Garimella, S., Bartosiewicz, Y., 2015. Computational and experimental analysis of supersonic air ejector: Turbulence modeling and assessment of 3D effects. International Journal of Heat and Fluid Flow 56, 305 – 316.

Moody, F.J., 1975. Maximum discharge rate of liquid-vapor mixtures from vessels. NEDO–21052 .

Palacz, M., Haida, M., Smolka, J., Nowak, A.J., Banasiak, K., Hafner, A., 2017a. HEM and HRM accuracy comparison for the simulation of CO_2 expansion in two-phase ejectors for supermarket refrigeration systems. Applied Thermal Engineering 115, 160 – 169.

Palacz, M., Smolka, J., Fic, A., Bulinski, Z., Nowak, A.J., Banasiak, K., Hafner, A., 2015. Application range of the HEM approach for CO_2 expansion inside two-phase ejectors for supermarket refrigeration systems. International Journal of Refrigeration 59, 251 – 258.

Palacz, M., Smolka, J., Kus, W., Fic, A., Bulinski, Z., Nowak, A.J., Banasiak, K., Hafner, A., 2016. CFD-based shape optimisation of a CO2 two-phase ejector mixing section. Applied Thermal Engineering 95, 62 – 69.

Palacz, M., Smolka, J., Nowak, A.J., Banasiak, K., Hafner, A., 2017b. Shape optimisation of a two-phase ejector for CO2 refrigeration systems. International Journal of Refrigeration 74, 212 – 223.

Park, C., Cho, H., Lee, Y., Kim, Y., 2007. Mass flow characteristics and empirical modeling of R22 and R410A flowing through electronic expansion valves. International Journal of Refrigeration 30, 1401–1407.

Pianthong, K., Seehanam, W., Behnia, M., Sriveerakul, T., Aphornratana, S., 2007. Investigation and improvement of ejector refrigeration system using computational fluid dynamics technique. Energy Conversion and Management 48, 2556 – 2564.

Pourmahmoud, N., Najafpour, H., Heidarpour, V., Rezazadeh, S., 2011. Computational fluid dynamics modeling of the turbulent flow in the expansion valves. Australian Journal of Basic and Applied Sciences 5, 51–60.

Rusly, E., Aye, L., Charters, W.W.S., Ooi, A., 2005. CFD analysis of ejector in a combined ejector cooling system. International Journal of Refrigeration 28, 1092 – 1101.

Saleh, B., Aly, A.A., 2016. Artificial neural network models for depicting mass flow rate of R22, R407C and R410A through electronic expansion valves. International Journal of Refrigeration 63, 113–124.

Sallet, D.W., 1991. Critical mass flow rates through pressure relief valves. Wärme - und Stoffübertragung 26, 315–321.

Shanwei, M., Chuan, Z., Jiangping, C., Zhiujiu, C., 2005. Experimental research on refrigerant mass flow coefficient of electronic expansion valve. Applied Thermal Engineering 25, 2351–2366.

Smolka, J., Bulinski, Z., Fic, A., Nowak, A.J., Banasiak, K., Hafner, A., 2013. A computational model of a transcritical R744 ejector based on a homogeneous real fluid approach. Applied Mathematical Modelling 37, 1208–1224.

Städtke, H., 2006. Gasdynamic aspects of two-phase flow: hyperbolicity, wave propagation phenomena and related numerical methods. Wiley-VCH.

Tong, L.S., Tang, Y.S., 1997. Boiling Heat Transfer and Two-Phase Flow. Taylor & Francis.

Varga, S., Soares, J., Lima, R., Oliveira, A.C., 2017. On the selection of a turbulence model for the simulation of steam ejectors using CFD. International Journal of Low-Carbon Technologies 12, 233–243.

Yazdani, M., Alahyari, A.A., Radcliff, T.D., 2012. Numerical modeling of two-phase supersonic ejectors for work-recovery applications. International Journal of Heat and Mass Transfer 55, 5744–5753.

Zhifang, X., Lin, S., Hongfei, O., 2008. Refrigerant flow characteristics of electronic expansion valve based on thermodynamic analysis and experiment. Applied Thermal Engineering 28, 238 – 243.

Zucker, R.D., Biblarz, O., 2002. Fundamentals of Gas Dynamics. John Wiley & Sons.